Indirect Observations of Electric Fields at Comet 67P

Anja Moeslinger[1], Hans Nilsson[1], Gabriella Stenberg Wieser[1], Herbert Gunell[2], and Charlotte Goetz[3]

[1]Swedish Institute of Space Physics
[2]Umeå University
[3]Northumbria University

June 11, 2023

Abstract

No spacecraft visiting a comet has been equipped with instruments to directly measure the static electric field. However, the electric field can occasionally be estimated indirectly by observing its effects on the ion velocity distribution. We present such observations made by the Rosetta spacecraft on 19th of April 2016 when comet 67P was at a low outgassing rate and the plasma environment was relatively homogeneous. The ion velocity distributions show the cometary ions on the first half of their gyration. We estimate the bulk drift velocity and the gyration speed from the distributions. By using the local measured magnetic field and assuming an E x B drift of the gyrocentre, we get an estimate for the average electric field driving this ion motion. We analyse a period of 13h, during which the plasma environment does not change drastically. We find that the average strength of the electric field is 0.21mV/m. The direction of the electric field is mostly anti-sunward. This is in agreement with previous results based on different methods

Indirect Observations of Electric Fields at Comet 67P

A. Moeslinger[1,2], H. Nilsson[1,2], G. Stenberg Wieser[1], H. Gunell[2], C. Goetz[3]

[1]Swedish Institute of Space Physics, 981 28 Kiruna, Sweden
[2]Department of Physics, Umeå University, 901 87 Umeå, Sweden
[3]Department of Mathematics, Physics and Electrical Engineering, Northumbria University, Newcastle-upon-Tyne, United Kingdom

Key Points:

- Rosetta observations show partial ring distributions of cometary ions at comet 67P.
- From the velocity distributions the plasma bulk velocity and gyration speed are determined.
- We estimate the electric field from the bulk velocity and find a mostly anti-sunward field of 0.21 mV/m.

Corresponding author: A. Moeslinger, `anja.moeslinger@irf.se`

Abstract

No spacecraft visiting a comet has been equipped with instruments to directly measure the static electric field. However, the electric field can occasionally be estimated indirectly by observing its effects on the ion velocity distribution. We present such observations made by the Rosetta spacecraft on 19th of April 2016 when comet 67P was at a low outgassing rate and the plasma environment was relatively homogeneous. The ion velocity distributions show the cometary ions on the first half of their gyration. We estimate the bulk drift velocity and the gyration speed from the distributions. By using the local measured magnetic field and assuming an $\mathbf{E} \times \mathbf{B}$ drift of the gyrocentre, we get an estimate for the average electric field driving this ion motion. We analyse a period of 13 h, during which the plasma environment does not change drastically. We find that the average strength of the electric field is 0.21 mV/m. The direction of the electric field is mostly anti-sunward. This is in agreement with previous results based on different methods.

Plain Language Summary

Measuring the static electric field in space plasmas is difficult. Most spacecraft do not have dedicated instruments for it, and the Rosetta mission to comet 67P is no exception. But the electric field is one of the main governing factors behind for the motion of newly born cometary ions. In this study, we use measurements of the cometary ions to estimate the average electric field close to the nucleus. The observations are made on the 19th of April 2016 by the Ion Composition Analyzer (ICA), which measures the energy and travel direction of the different plasma species. The specific shape of the observed velocity distribution of cometary ions – a partial ring – indicates that the fields accelerating the observed cometary ions are relatively homogeneous. The spatial scale this applies to is approximately one gyroradius, which we estimated to be around 340 km. The resulting electric field is 0.21 mV/m, which is significantly smaller than the expected field in the upstream solar wind, far away from the nucleus.

1 Introduction

The atmospheres of comets are produced by the sublimation of ice near the nucleus' surface. During this sublimation, the ice (primarily water and CO_2) also lifts off dust from the nucleus surface. Cometary dust is usually comprised of organic and rocky material (Filacchione et al., 2019). The intensity of this process is quantified as the outgassing or production rate. It is modulated by the strength of the solar irradiation at the comet's position, and depends on the size and composition of the comet itself. The outgassing rate therefore varies along the comet's elliptical trajectory, and even more so between different comets. Due to the low mass of the comet nucleus (in comparison to e. g. planets) the atmosphere is gravitationally unbound and expands freely into space (Bieler et al., 2015). Some of the molecules in this atmosphere become ionised by EUV flux or electron-impact-ionisation and form a plasma cloud of newborn cometary ions (Galand et al., 2016). The newborn ions are accelerated by the electromagnetic fields around the nucleus. These fields are the result of the interaction between the solar wind and the cometary plasma cloud (Nilsson et al., 2021).

In the comet reference frame the solar wind travels with a speed of around 400 km/s in the anti-sunward direction. In combination with the frozen-in magnetic field this creates a convective electric field at the comet. Newborn ions are accelerated in direction of the electric field in a process often referred to as ion pick-up. The accelerated ions are called pick-up ions. They gyrate due to the magnetic field and gain energy due to the electric field. The relative size of the plasma environment can be characterised by comparing it to the gyroradius of the ions. If the plasma environment is much larger than the ion gyroradius, fluid dynamics is appropriate to describe the main physical processes, as in the example of comet 1P/Halley. Once the plasma environment is of a similar spatial scale as the ion gyroradius, kinetic effects have to be taken into account. This is the case for comet 67P, especially at a low outgassing rate far away from the Sun (Goetz et al., 2022).

Under typical solar wind conditions, the gyroradius of cometary water ions is on the order of ten thousand kilometres. If the spatial scale of the plasma interaction region between the solar wind and the comet is much larger than this gyroradius, the pick-up ions form ring distributions in velocity space. Such distributions were observed during the fly-by of the Giotto spacecraft at comet 1P/Halley (Reinhard, 1987). By pitch-angle scattering these rings can evolve into shell distributions. The gyrocentre of the distributions is the solar wind velocity component perpendicular to the magnetic field (Coates et al., 1989). The ring and shell distributions were observed essentially everywhere in the coma of 1P/Halley, from 5 million kilometres away from the nucleus to the the bow shock (Neugebauer et al., 1989). Additionally, enhancements in the power spectra of the magnetic field at the water ion cyclotron frequency were observed (K. Glassmeier et al., 1987). This is the same frequency the water ions gyrate with when forming ring and shell distributions.

A very different situation is present at comet 67P/Churyumov-Gerasimenko (hereafter: comet 67P), target of the Rosetta mission (K.-H. Glassmeier, Boehnhardt, et al., 2007). The outgassing rate of comet 67P is much lower than 1P/Halley, even at perihelion. As a consequence, the spatial scales of the plasma environment are also much smaller. Because the Rosetta spacecraft was usually orbiting the comet at walking speed relatively close to the nucleus, the nature of the observations are very different compared to Giotto observations. The observations in the terminator plane probe the plasma environment of the newborn cometary pickup ions. The evolution to full ring and shell distributions is expected to happen much further downstream, in the tail of comet 67P (Williamson et al., 2022).

Estimating the gyroradius close to the nucleus is difficult, as it requires knowledge about the electric field. Previously, estimations of the electric field direction were based on the assumption that the ions are unmagnetised, and are therefore accelerated and flowing along the electric field (Nilsson et al., 2018). This method only gives the direction of the field, not it's strength. If the ion gyroradii are very large, the assumption of unmagnetised ions holds. The ions are observed as uni-directional. Rosetta has no dedicated instruments that are capable of measuring the static electric field with sufficient accuracy. However, the velocity distribution of cometary pick-up ions gives us information about the plasma environment close to the nucleus. If we observe the beginning of a gyration in the velocity distribution of cometary ions we can characterise the electric field and gyroradius close to the nucleus. In this paper, we present observations of partial ring distributions in the cometary pick-up ion data, and show how they relate to the electric fields around the comet.

2 Instrument Description

To derive the ion velocity distributions of the cometary plasma environment, we use data from the Ion Composition Analyzer (ICA), part of the Rosetta Plasma Consortium (RPC; Carr et al., 2007). In addition to that, we use magnetic field measurements from the magnetometer MAG, also part of the RPC instrument package. Both instruments are described below. More information about RPC can be found in the RPC User Guide (Beth et al., 2019).

2.1 Ion Composition Analyzer

ICA was designed to measure the velocity distributions of the major positive ion species around comet 67P (Nilsson et al., 2007). The mass resolution of the instrument allows us to distinguish between protons (H^+), alpha particles (He^{2+}), He^+, and heavier ions, such as H_2O^+ and CO_2^+. The energy range covers low energy ions at a few eV/q up to energies of 40 keV/q. There are 96 energy bins in total, which are logarithmically spaced.

The nominal instrument field-of-view is $360° \times 90°$ (azimuth × elevation). This angular field-of-view is subdivided in 16 azimuth and 16 elevation angles. An individual pixel in this 16×16 grid has therefore a nominal size of $22.5° \times 5.625°$. All 16 azimuth directions are measured simultaneously. The different elevations are measured in sequence. The full energy range is measured for each elevation. A full measurement cycle covering all elevations and energies, also referred to as "scan", takes 192 s. Due to the limited resolution of the instrument's high voltage supply the elevation angles at low energies (up to approximately 100 eV/q) depend on the measured energy. This results in a changing pixel boresight at different energies. To compensate for this effect, we resample the elevation angles of each azimuth sector into 17 equally-spaced angles that cover the nominal 90° elevation. Parts of the ICA field-of-view are obstructed by the spacecraft and solar array, but this is not expected to affect the results shown here. In this study we use the L4-PHYSMASS dataset, which contains differential flux for H^+, He^{2+}, and heavier ions.

2.2 Magnetometer

The magnetometer MAG consists of two triaxial fluxgate magnetometers that are mounted on a spacecraft boom. The measurement range is ±16 384 nT in each direction, with a resolution of 20 bit (31 pT). The vectors are sampled with a frequency of 20 Hz (K.-H. Glassmeier, Richter, et al., 2007). For the purpose of this study, we average the magnetic field data over the duration of one ICA scan, which eliminates high-frequency disturbances. There is a remaining unknown offset in the data due to temperature drifts of the instrument. This offset is of the order of a few nT for each axis, and can affect the magnitude and direction estimate of the magnetic field. With a typical measured magnetic field strength of 20 nT the error is expected to be below 15° for the time period considered in this study.

3 Methods

The starting point for our analysis is the velocity distribution of cometary pickup ions. To quantify and interpret them we apply a ring fitting procedure to the observed energetic cometary ion population. The resulting fitted velocities are projected into a coordinate system that is decoupled from changes in the plasma environment (e. g. a change in magnetic field direction) for better comparison between the individual scans. From the fitted velocities we can derive an estimate for the average electric field.

3.1 Ring Fitting

As we will show in section 4, there is an energy-angle dispersion in the distribution of cometary ions. We use a ring fitting procedure to estimate the bulk flow properties of the energetic cometary plasma. This procedure is presented in Moeslinger et al. (2023), but in this study we apply it to the dataset of cometary pickup ions. We will outline the main algorithm and its limitations below.

In a first step, we estimate the plane that contains the data. This plane corresponds to the gyration plane of the particles, which is perpendicular to the estimated magnetic field direction. From this step we get the parallel (to the magnetic field) bulk flow velocity $\mathbf{u}_{\text{bulk},\parallel}$. Normalising this vector gives the unit vector $\mathbf{r}_{\text{bulk},\parallel}$, which is the plane normal. In the second step we fit a sphere to the data, with the constraint that the centre of the sphere must lie on the plane determined in the first step. The intersection of both results gives a circle with a radius that corresponds to the gyration velocity $u_\perp$. The offset between the fitted centre of the sphere and $\mathbf{u}_{\text{bulk},\parallel}$ is the drift velocity of the bulk plasma $\mathbf{u}_{\text{bulk,drift}}$. In both steps we use a weighted non-linear least squares fitting algorithm. More information can be found in Moeslinger et al. (2023). The fitting is done individually for each ICA scan. The velocity vectors used for fitting are the median energy vectors of the cometary ions for each azimuth/elevation pixel. As we are interested in the pickup ion population, the energy bins below 40 eV are excluded from the analysis. These low energy ions typically belong to a different ion population with a different flow direction (see Berčič et al., 2018; Nilsson et al., 2020). We also discard pixels with zero flux. The median energy is defined as the energy bin where the flux integrated in energy from 40 eV up to this bin exceeds 50 % of the total flux of the pixel. This median energy is converted to velocity vectors assuming a water ion plasma. The logarithm of the total flux for each vector is used as a weight parameter for the fitting procedure.

3.2 Projections

The fitted velocity parameters obtained by the the algorithm in Section 3.1 are in ICA instrument coordinates. Due to the low spacecraft velocity with respect to the comet (of the order of a few m/s) this is essentially the rest frame of the comet nucleus. However, the alignment of the instrument coordinate system is arbitrary with respect to the plasma flow. Therefore, we define a new coordinate system, which is determined individually for each scan. In this system:

1. The z-axis is aligned with the direction of $\mathbf{u}_{\text{bulk},\parallel}$. This reduces the gyration to the x-y plane. To ensure a consistent gyration direction for all scans, the sign is determined by the local magnetic field (i. e., $\hat{\mathbf{z}} \cdot \mathbf{B} > 0$).
2. The x-axis is the sunward direction, projected onto the gyration plane.
3. The y-axis completes the right-handed system.

This coordinate system decouples the observed ion distribution from changes in the plasma environment, such as the magnetic field direction. The resulting fitted velocities can be compared in both magnitude and direction over longer timescales. It also allows for an easier analysis of the velocity distributions and the accuracy of the fitting procedure. For this purpose, we project the measured data into a cartesian velocity grid, converting them to velocity vectors assuming a mass per charge of 18 amu/q (single charged water ions) as above. In this reference frame, the x-y projection contains the velocity distribution information that shows the gyration pattern of the ions.

3.3 Electric Field

The drift velocity in the gyration plane determined from the ring fits, $\mathbf{u}_{\text{bulk,drift}}$, is the result of electric fields around the comet. If we assume that the electric and magnetic fields are homogeneous over the relevant spatial scales, the drift velocity is given by:

$$\mathbf{u}_{\text{bulk,drift}} = \frac{\mathbf{E} \times \mathbf{B}}{B^2} \qquad \Rightarrow \qquad \mathbf{E} = -\mathbf{u}_{\text{bulk,drift}} \times \mathbf{B} \tag{1}$$

To fully utilise the information obtained by the ring fitting procedure, we only use the z-component of the measured local magnetic field vector. This is the component along the estimated parallel bulk flow of the cometary plasma, and the estimated electric field is confined to the gyration plane.

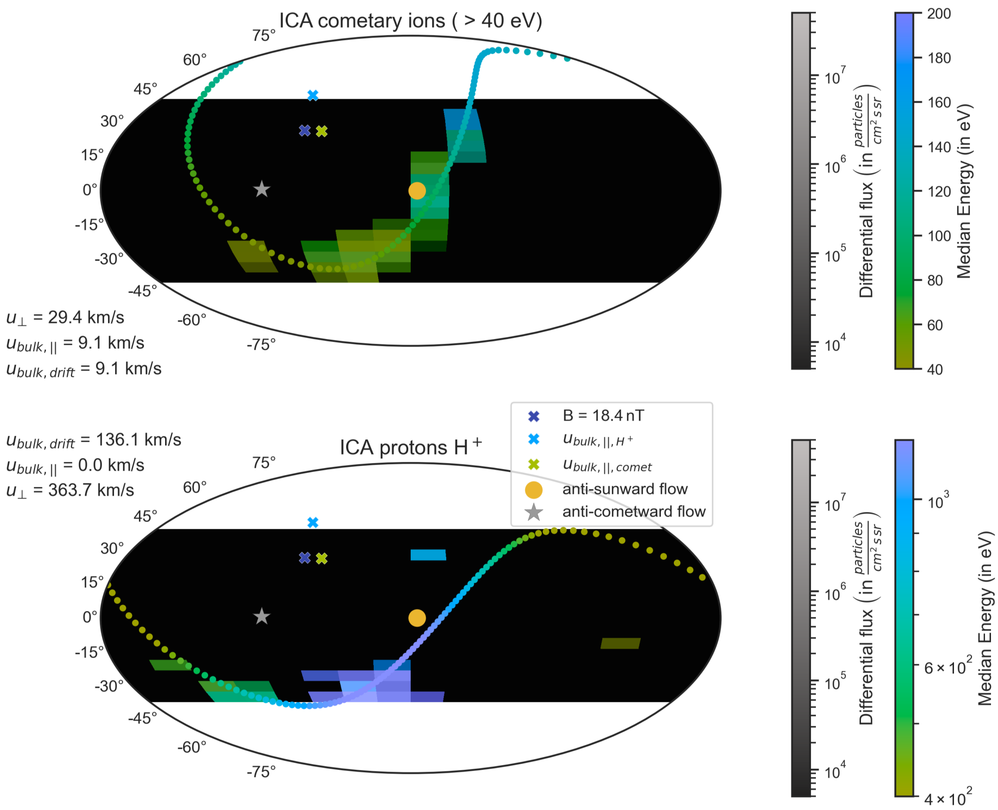

Figure 1. Dual colourmap plots of the cometary ions (top panel) and the solar wind protons (bottom panel). The background shows one ICA scan, taken at 06:38:24. No particle flux was detected for the black pixels. The white areas are not covered by the ICA field-of-view. The dots in both panels show the result of the ring fitting procedure for each species. For more information see text..

4 Results

We present results from a case study using data from April 19th, 2016, when comet 67P was at a heliocentric distance of 2.8 AU. Only the time period between 00:00 - 13:00 is included. This is the same time period as analysed in Moeslinger et al. (2023). The rest of the day exhibits strong fluctuations in the magnetic field as well as spacecraft manoeuvres and is therefore not suitable for studying partial ring distributions.

4.1 Velocity Distributions of Cometary Ions

Any distribution with a large angular spread may partially fall outside the field-of-view of the instrument. To monitor these limitations, we assess the measured velocity distributions directly in instrument coordinates, as shown in Figure 1. The upper panel shows the cometary ions with energies above 40 eV. Protons are shown in the lower panel. The plots visualise the median energy as the hue of each pixel, and the differential flux, integrated over the entire energy range considered, as its intensity. More information on this visualisation method and a discussion of the solar wind protons can be found in Moeslinger et al. (2023).

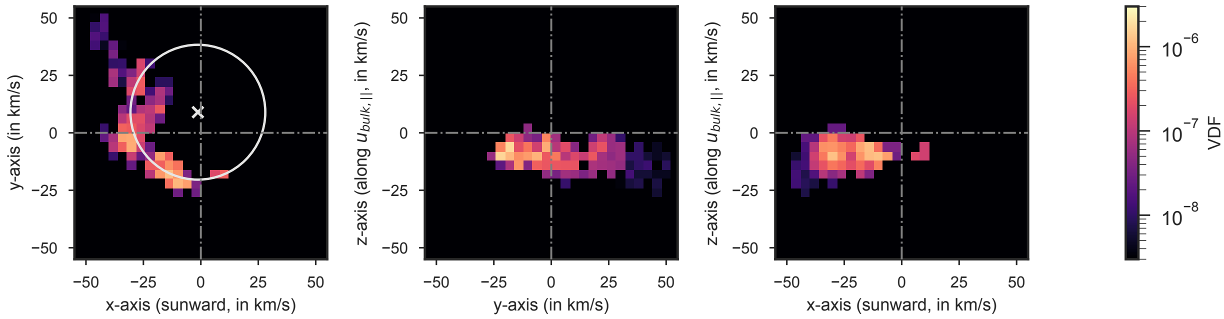

Figure 2. Projected velocity distributions of the cometary ions. The data is the same as shown in Figure 1, but converted to velocity and projected into a cartesian coordinate system. The colourbar shows the velocity distribution function (VDF) of each bin. The z-axis is aligned with the estimated parallel direction ($u_{\mathrm{bulk},\|}$) and oriented almost parallel to the local measured magnetic field. The x-axis is the component of the sunward direction perpendicular to the z-axis, and the y-axis completes the right-handed system.

Figure 1 shows a typical example of the distributions of cometary and solar wind ions during one ICA scan. ICA does not cover elevations exceeding ±45° (white areas). The energy-angle dispersion is clearly visible in both populations. In case of the cometary ions, the highest observed median energies are around 150 eV. The results of the ring fitting procedure are indicated by the dots, colour-coded with the respective energy colour scale. The estimated normal vector of the gyration plane is indicated by the green (cometary ions) and light blue (protons) cross. The dark blue marker shows the magnetic field direction. Both normal vector estimates are within 15° of the local magnetic field measurement. The fitted velocities for the cometary ions are $u_{\mathrm{bulk,drift}} = 9.1\,\mathrm{km/s}$, $u_\perp = 29.4\,\mathrm{km/s}$, and $u_{\mathrm{bulk},\|} = 9.1\,\mathrm{km/s}$.

A different perspective of the same data is given in Figure 2. The measurements of each pixel were converted to velocities in a cartesian coordinate system, as described in Section 3. The three panels show the projections on the x-y, y-z, and x-z plane. The data is integrated over the third dimension. In panel a) the fitted ring and its centre, the estimated bulk drift velocity, are indicated. The fitted ring is a good approximation of the measured data. The lowest velocities in the gyration plane are about 20 km/s, which corresponds to the lower energy threshold at 40 eV. These low velocities are found in the direction opposite of the drift velocity. The maximum velocities are at around 40 km/s. These ions have completed a little less than half a gyration compared to the lowest energy ions. As there is no complete ring distribution, all observed ions are expected to be on their first gyration. The “side views” of the data, shown in panels b) and c), are quite flat and only spread horizontally. This indicates that the data is indeed mostly distributed on a plane, and the $\mathbf{r}_{\mathrm{bulk},\|}$ estimate is a good estimator of the plane. The parallel velocity component varies a few km/s around the fitted value of 9.1 km/s.

The data analysis shown in Figures 1 and 2 was done for a 13 h time period, from 00:00 - 13:00 on April 19th, 2016. There are a total of 225 ICA scans available during this period. A preliminary inspection of the cometary ion data as shown in Figure 1 (without the ring fitting) showed that 169 of these 225 scans are suited for a ring fitting algorithm. The scans excluded in this step either have too little data (e. g. only a few pixels contain any flux), or there is no clear energy-angle dispersion visible. The ring fit-

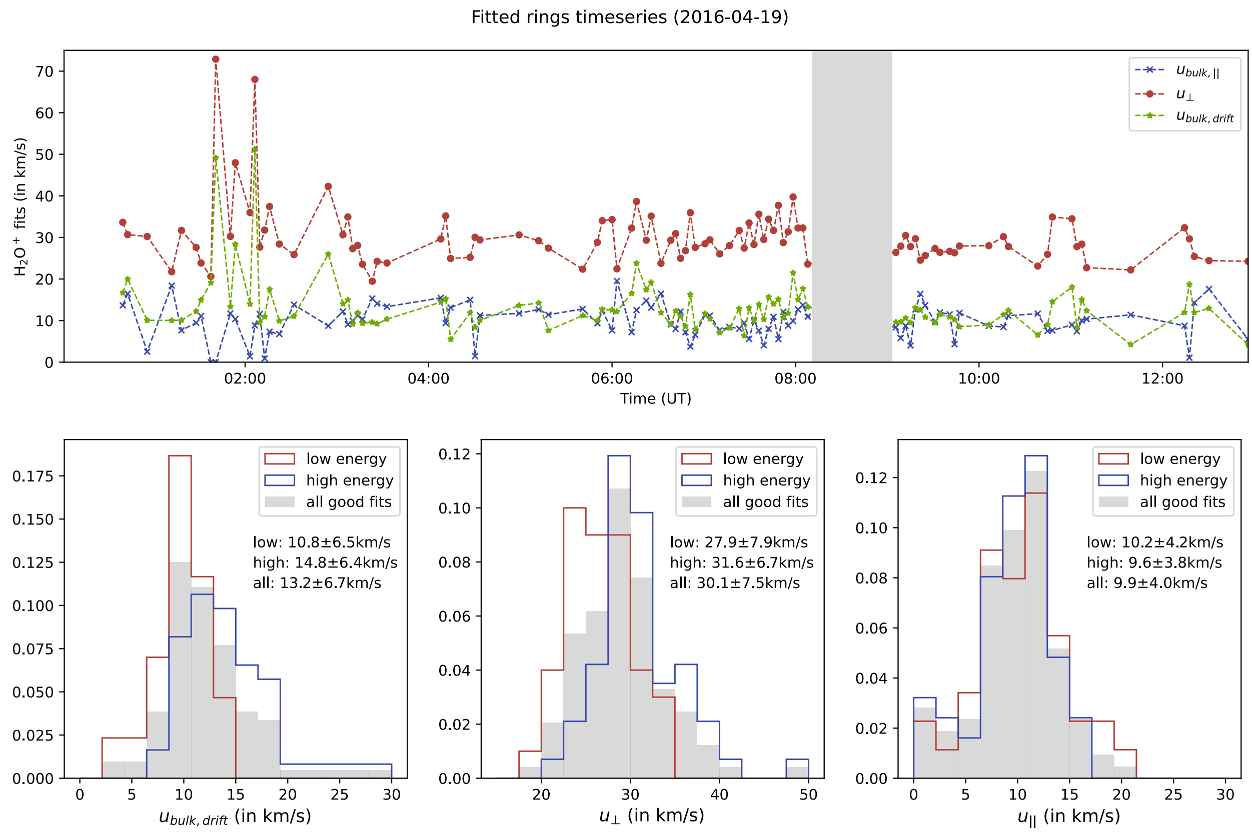

Figure 3. Resulting fitted velocities for 2016-04-19, from 00:00 – 13:00. Top row: timeseries of the three fitted velocities for cometary ions. Only the 99 good fits are included. No ICA data is available for the time indicated by the grey areas. Bottom row: histograms of the distribution of the fitted velocities for the same data as the top row. The left panel shows the bulk drift velocity. The middle panel shows the fitted gyration velocity $u_\perp$. The right panel shows the parallel velocity. The grey histograms show the distribution of all good fits. The red and blue histograms show the distributions of the good fits separated in scans with low and high energy range; see text for more details. All histograms are normalised. The y-axes are corresponding densities (arbitrary units). The text insets give the mean and standard deviation for each distribution.

ting algorithm yielded a successful fit in 99 of these 169 scans, based on visual inspection. The criteria for a successful fit include good agreement between data and fit in both angular space as well as energy. To analyse why the success rate was not higher, we performed a principal component analysis (PCA) of the underlying data. We found that the fitting algorithm works better for larger PCA variances (data not shown). We interpret this as a requirement for sufficient spread of the data points to give stability to the fitting procedure. If the points are distributed mostly along a straight line in 3D space, the plane this line lies on is not well defined. Only if the line deviates significantly from a straight line, as in the case of a partial ring with sufficient angular extent, the plane is well-defined. In this case, both the first and the second PCA component variance are sufficiently large. In the case of good fits, the third PCA vector aligned very well with the corresponding parallel vector estimate from the ring fitting procedure.

A timeseries of the resulting velocities can be seen in figure 3, top panel. The plot only includes good fits. The dominating velocity is the gyration speed $u_\perp$, with an average of 30.1 km/s. The magnitude of the bulk drift velocity is about half of the gyration speed. The average is 13.2 km/s. $u_{\mathrm{bulk,drift}}$ and $u_\perp$ are correlated. The parallel bulk velocity is usually the smallest of the three (average: 9.9 km/s), and does not correlate with the other two.

The statistical distribution of the three fitted velocity components can be seen in the bottom row of Figure 3. The grey histograms show the normalised distribution of all good fits for each velocity component. The distributions of $u_{\mathrm{bulk,drift}}$ and $u_\perp$ are roughly gaussian-shaped, with slightly elongated tails towards higher velocities. The standard deviations of the distributions are very similar, with 6.7 km/s and 7.5 km/s for $u_{\mathrm{bulk,drift}}$ and $u_\perp$, respectively. The distribution of $u_{\mathrm{bulk},\parallel}$ does not have a high velocity tail. Instead, there is a slight increase for very low velocities. This is because the fitting procedure effectively gives the absolute value of the parallel component. Any negative values in a fixed frame (e. g. B-field aligned) are mapped onto their positive counterparts, creating this artificial peak at velocities close to zero.

Inspecting all individual gyration patterns (as shown in Figure 2) we noticed a change when the maximum energy observed is higher. Therefore, we divided the good fits into two categories: "high energy" and "low energy" scans. The "high energy" scans contain pixels where the median energy exceeds 200 eV. This is the case for 58 out of the 99 good fits, for the remaining 41 scans the median energy of every pixel is below 200 eV. Both $u_{\mathrm{bulk,drift}}$ and $u_\perp$ have the distribution shifted towards higher velocities for the high energy scans, compared to the low energy scans. The distribution of $u_\parallel$ on the other hand appears almost identical for both cases.

4.2 Electric Fields

We can use the fitted drift velocity of the plasma bulk flow to get an estimate of the average electric field. The magnetic field used to calculate the electric field (according to Equation 1) is the $\mathbf{r}_{\mathrm{bulk},\parallel}$-aligned component of the average measured magnetic field for each scan. The results are projected into the same coordinate system used for Figure 2. This way, we can compare the scans in a statistical manner.

Figure 4 shows the electric field estimates of all good fits, split up into high energy and low energy scans. The plot shows the x-y plane, which contains all necessary information. As the magnetic field is exclusively along the z-axis in this frame the z-component of the electric field is zero. The electric field is dominated by an anti-sunward component for all scans. It ranges from −0.05 mV/m to −0.35 mV/m along E_x. The mean is −0.2 mV/m. The high energy scans show a larger E_x component, with a mean of −0.23 mV/m, compared to the low energy scans (mean: −0.15 mV/m). No such dependence on the energy range can be identified in the E_y component. It ranges from 0.05 mV/m to −0.25 mV/m, with a mean of −0.06 mV/m. The distributions along E_x and E_y are also shown by the histograms on top and left of the main figure. The similarity of the high and low energy distributions for the E_y component is evident. A tendency towards stronger anti-sunward fields for high energy scans can also be identified in the E_x-histogram.

The inset on the upper left corner shows the distribution of the magnetic field strength used for calculating the electric field. Overall, the distributions for the high and low energy cases are very similar. There is no favour towards higher magnetic fields for the high energy cases that could influence the results of the electric field estimate. The second inset shows the magnitude of the E-field estimate. There is a tendency for higher electric field strengths for the high energy scans as well, but it is not as pronounced as for E_x.

A timeseries of the same dataset as in Figure 4 is shown in Figure 5. Until 03:00 the E-field estimates vary significantly, both between individual scans and over time. After 03:00 the variability over time becomes less. There is another clearly noticeable peak

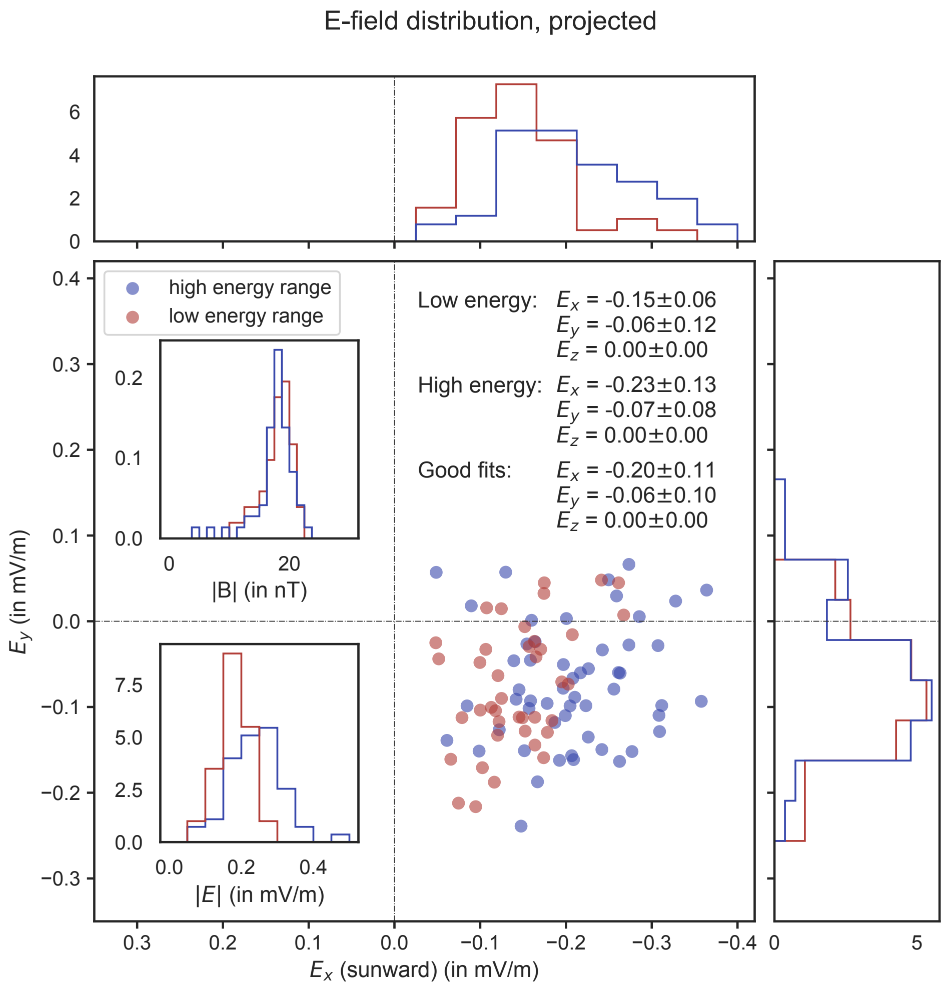

Figure 4. Distribution of the electric field estimates. Only the good fits, split up between high and low energy range scans, are included. The results are projected into the same cartesian coordinate system as used in Figure 2. The magnetic field used for the calculation of the E-field estimate is the z-component of the measured magnetic field (in this cartesian coordinate system). The inset in the upper left corner shows a histogram of the magnitude of the magnetic field. In the lower left corner another inset shows the distribution of the E-field along the z-axis. The text gives the statistical properties of the individual distributions (all values in mV/m). For more information see text.

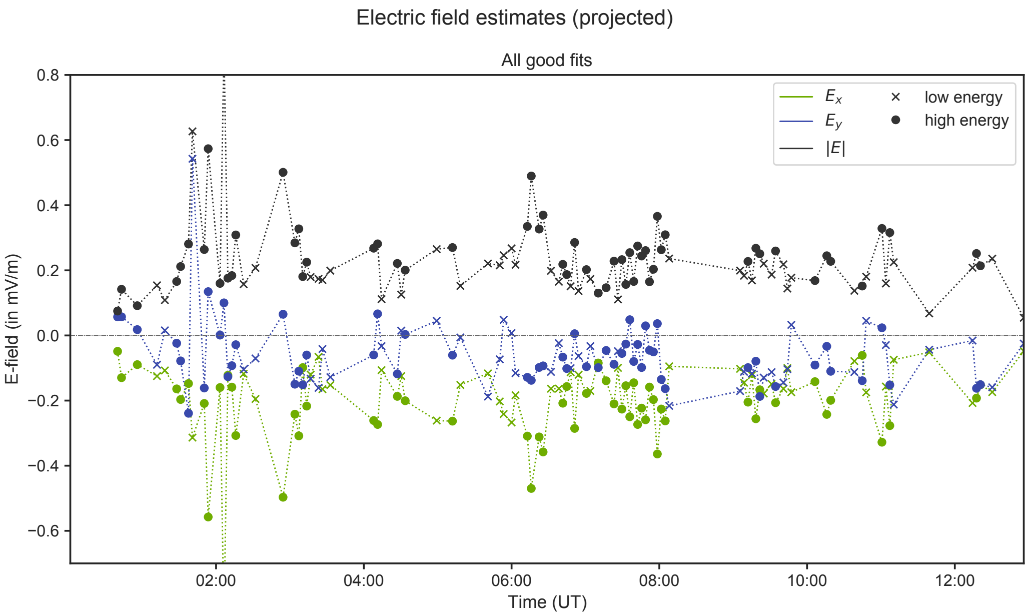

Figure 5. Timeseries of the estimated electric field. The coordinate system for the individual components is the same as used for Figures 2 and 4 (i. e., E_x is sunward in the gyration plane). The E_x and E_y components as well as the magnitude are displayed. The E_z-component is zero for all scans and therefore not shown. Different markers indicate whether the estimate belongs to a high (circle) or a low (cross) energy scan.

around 06:00. An anti-sunward electric field component (negative E_x) dominates the total electric field in almost all cases. The occurrence of high or low energy scans does not show consistent patterns over time. During some periods there are several consecutive scans of the same type, for example around 06:00, and between 07:00-08:00. After 09:00 on the other hand, the high and low energy scans alternate almost every successful fit.

5 Discussion

As shown in Figure 1 there is a clear energy-angle dispersion visible in the cometary ions above 40 eV. Such partial ring distributions can only form in a plasma environment with sufficiently homogeneous electric and magnetic fields. Of the observed particles, the most energetic ones have completed almost half a gyration, so the ions cannot be regarded as unmagnetised. However, the spatial scale of the interaction region is not large enough for the formation of fully developed rings. If the fields were heterogenous there would be more randomness in the ion velocity distribution pattern and the partial rings would be smeared out. Occasionally, some energetic ions with energies far above 200 eV occur outside of the partial ring pattern (not shown). We believe that these are born outside the homogeneous interaction region, possibly in a region that is more dominated by the solar wind given their high energies. These random high-energy ions usually interfere with the ring fitting procedure and are therefore excluded from the results.

From the fitted rings we can deduce the bulk flow of the energetic cometary plasma (see Section 5.1). The obtained fitting parameters can also be used to infer other quantities of the plasma environment. With the gyration speed $u_\perp$ we can estimate the gyroradius of the particles. The drift velocity in the gyration plane $\mathbf{u}_{\mathrm{bulk,drift}}$ gives us an estimate for the electric field strength and direction. This is discussed in further detail in Section 5.2.

5.1 Velocity Distributions

There are no significant changes in the spacecraft pointing with respect to the sunward and cometward directions during the considered time period. However, the same cannot be said for the plasma environment. Even if the fields are homogeneous, they can slowly change over time. This can easily be seen in the change of the locally measured magnetic field from scan to scan, but is equally applicable to the electric field. To quantify the changes in the plasma environment we analysed the variability of the magnetic field as well as the fitted $\hat{\mathbf{r}}_{\mathrm{bulk},\parallel}$. For each scan with a good fit we looked at the angle between the direction and the average direction over the entire observation period. The angular variability relative to the measured magnetic field is on average 18°, but even exceeds 30° in multiple cases. The variability relative to the mean in the direction of $\hat{\mathbf{r}}_{\mathrm{bulk},\parallel}$ are slightly less, with an average of 12.5° (good fits only). Deviations above 30° are possible in this case as well. A static coordinate system is therefore not suitable. Instead we used the $\hat{\mathbf{r}}_{\mathrm{bulk},\parallel}$ estimate to calculate the projection as described in Section 3.2. In this coordinate system the bulk drift velocity and electric field estimates of the individual scans can be systematically compared over the entire observation period.

In the simplest theoretical case of ion pickup in a homogeneous plasma, for example in the undisturbed solar wind, the ratio between the gyration speed and the drift speed is 1. This is a direct consequence of the ions being introduced into the system with 0 velocity. The average speed is the drift speed as determined by the background electric field, but the maximum speed of the particle is twice that. In our case the ratio $u_{\perp}/u_{\mathrm{bulk,drift}}$ is 2.3 for all good fits, 2.1 for the high energy scans, and 2.6 for the low energy scans. Consequently, the minimum speed of the particles gyrating along the fitted rings never reaches 0. Drift velocities of approximately 13 km/s further indicate that the observed velocity distributions are not directly caused by ion pickup in the undisturbed solar wind electric field. For this case, drift velocities of the order of 400 km/s are expected. We rather see pick-up in a region that is mostly shielded from the solar wind electric field and consequently has a lower drift speed.

An estimate for the spatial scales of the interaction region that forms the observed partial rings is the gyroradius of the cometary ions: $r_g = \frac{mu_{\perp}}{qB}$. The gyroradius is defined in the electric-field-free reference frame. Due to the lack of knowledge about the electric field strength it usually cannot be calculated properly at comet 67P. We get the required gyration speed $u_{\perp}$ directly from our fitted rings. The mass m and charge q are assumed to be 18 amu and 1.6×10^{-19} C (singly charged water ions). For the magnetic field we use the z-component of the locally measured magnetic field in the projected coordinate system. The average gyroradius for all good fits is 340 km. High energy scans have on average a larger gyroradius (364 km) than low energy scans (306 km). We therefore expect the interaction region in which the rings are formed to be somewhat larger for the case of high energy scans. These values are much smaller than the expected gyroradii in the undisturbed solar wind (approx. 10 000 km). At the same time, they are much larger than the distance between the spacecraft and the nucleus (35 km). The observed ions, especially those with higher energies that have completed more than a quarter of a gyration, must therefore originate from an area further away from the nucleus than the Rosetta spacecraft.

Apart from some large fluctuations in the beginning of the day, the variation in the magnitude of all three fitted velocities are rather small (see Figure 3). Some differences in the mean values of the individual distributions of high and low energy scans are found. No significant differences in the standard deviations of the distributions between the high energy scans and the low energy scans are found. The uncertainties in the measured energy due to the limited energy resolution of the instrument and the derived velocity estimate may contribute to this spread in the fitted velocities. The energy bin width of ICA increases with higher energies, potentially increasing the spread of the distribution when higher energies are measured. As we see no such increase from low to high energy range scans in the results, the main contributing factors to the spread are uncertainties from the fitting procedure and the actual variations in the ion distribution over time. Occurrence of the latter is supported by the observations e. g. around 03:00 and between 07:00 - 08:00 where the estimates of $u_{\mathrm{bulk,drift}}$ and $u_{\perp}$ increase/decrease consistently over several successful fits. Visual inspection of the observed and projected distribution functions (Figures 1 and 2, but for the entire observation period) revealed that there are changes in the velocity distribution function on the timescales of individual scans. This includes both changes in the shape of the distribution, as well as changes in the direction of the drift velocity. These changes are not exclusively due to a change in the magnetic field direction because they also appear in the projected velocity distributions. We think that these variations are actual changes in the ion distributions and the entire plasma environment over time.

The parallel velocity component $\mathbf{u}_{\mathrm{bulk},\parallel}$ may be the result of an acceleration along the magnetic field. It may also result from an initial acceleration perpendicular to the magnetic field followed by a change of the magnetic field direction. Such a change of direction is expected around the nucleus due to field line draping. The direction of $\mathbf{u}_{\mathrm{bulk},\parallel}$ gives us an estimate of the upstream magnetic field direction on a spatial scale of the gyroradius. The estimate of $\left|\mathbf{u}_{\mathrm{bulk},\parallel}\right|$ is not well correlated with the $|\mathbf{u}_{\mathrm{bulk,drift}}|$ estimate. This indicates that the mechanisms responsible for acceleration in the gyration plane and perpendicular to it are not coupled. The ambipolar electric field, which is only strong close to the comet nucleus (Vigren & Eriksson, 2019), can provide such an acceleration mechanism. However, as our estimation method relies on the magnetic and electric fields being perpendicular, we cannot characterise the magnetic field-aligned component.

For a larger statistical analysis of cometary pickup ion populations PCA may provide a more efficient way to detect the occurrence of partial ring distributions. A sufficient variance of the individual principal components seems to be a requirement for successful ring fitting. An automated pre-selection based on this criterium will make the assessment of large datasets more feasible than visual inspection alone. Furthermore the last principal component estimate can directly be used as an estimate for the parallel flow direction. This may speed up the fitting procedure, and can also be used to directly calculate the projections for visualisation purposes.

5.2 Electric fields

The local electric field at the comet is important in many ways. It accelerates the newborn ions. Without electric fields, the ions can only change their direction through gyration, not their energy. The gyroradius of newborn ions can only be calculated if we know the electric field in their rest frame. The change between the upstream solar wind electric field and the local cometary electric field shows how shielded the cometary plasma cloud is from the solar wind electric field. In general, wave electric fields can also provide energy to the ions through wave-particle interaction. This mechanism usually happens at frequencies larger than the available time resolution of the ion measurements and can therefore not be assessed with the results presented here.

The anti-sunward component almost always dominates the electric field estimates. This component is larger for the high energy range scans. We identified two possible explanations:

1. The overall electric field strength at the comet is larger for the high energy range scans.

2. The high energy range scans include ions from a larger area around the comet with higher electric fields.

Because the spatial scales for the low energy case are smaller (see gyroradius calculation above) and the distance between spacecraft and nucleus is the same throughout all observations, the high energy scans also sample an area that is slightly further away from the comet nucleus compared to the low energy scans. If the second scenario is correct, this would imply an increase of the anti-sunward electric field further away from the nucleus. It also indicates that the fields are not completely homogeneous over the spatial scales affecting the observed ions. Goetz et al. (2017) provide an estimate for the homogeneity of the magnetic field with respect to cometocentric distance at low outgassing rates. For the solar wind parameters and comet outgassing rates seen in this study, their model predicts a quite stable magnetic field strength from the nucleus up to a distance of approximately 300 km. Further away the magnetic field drops quickly to the magnetic field strength of the undisturbed solar wind. These results indicate that the constant magnetic field assumption is true for about one gyroradius. Variations in the electric field estimate are unlikely to be caused by the magnetic field profile.

We can compare our results to other published electric field estimates for comet 67P at low activity levels. Nilsson et al. (2018) derive an electric field estimate for the entire Rosetta mission. Their estimate was based on a simple analytical model for a cylindrical comet plasma cloud and assumptions about the solar wind electric field. The pickup ion gyroradius was assumed to be much larger than the spatial scale of the cometary plasma. The results show large variabilities over time. For the time period in this study, the magnitude of the electric field estimate is between 0.1 mV/m and 0.8 mV/m. The direction deviates from the anti-sunward direction by 10° to 60°. Now, for the first time, we have estimates of the electric field directly derived from observations. Our results fall within the same range as the model based estimate, with a strong bias towards lower electric field strengths.

Gunell and Goetz (2023) used particle-in-cell modelling to determine the electric fields around the nucleus, and compared with an analytical electric-field model similar to the one in Nilsson et al. (2018). For computational reasons, the nucleus and the entire plasma environment were scaled down by a factor of 200. The fields presented are therefore much larger (up to 1 V/m) compared to reality and can only be compared to our results in direction, not strength. Very close to the nucleus the electric field has a strong anti-sunward component. This is partially retained in the downstream region. However, the convective electric field of the solar wind is the dominant component at 40 km and further away from the nucleus (scaled back to a "real" comet). The heliocentric distance of the comet in their paper is 3 AU, which is larger than in our case. This may explain some of the discrepancies, as the plasma cloud of cometary ions should be larger in our case. In addition to this, the particle-in-cell model uses heavy electrons ($m/m_e = 20$). This further disturbs the spatial scales of the plasma cloud.

In our case the gyroradius is small enough so we can observe a partial gyration of the cometary ions. The estimated drift velocity is perpendicular to the electric field, and the ions are partially magnetised. The resulting electric field is mostly anti-sunward. The same result was also found in previous publications, but in a very different scenario: it was inferred by the motion of the energetic pickup ions, which were travelling anti-sunward according to their calculated bulk velocity moments. This only provides an approximate estimate of the direction of the electric field in the case of very large gyroradii, where all observed energetic pickup ions are accelerated along the electric field. In this scenario, a gyration is not seen in the velocity distribution. If there is a substantial energy-angle dispersion, as in our case, the moment calculations may give inaccurate results. Only in the case of full rings can the bulk drift from moment calculations be used to properly estimate the drift velocity of the distribution.

6 Summary and Conclusions

In alignment with previous observations at Giotto (Coates et al., 1989), we find a clear partial ring-shaped distribution of cometary pickup ions in Rosetta data recorded at comet 67P. Our observations are made at low cometary activity. The plasma environment is much smaller than at 1P/Halley. Instead of fully developed ring distributions we observe newborn cometary ions on the first half of their gyration. These partial rings in velocity space are characterised by their gyration speed $u_\perp$, their bulk drift velocity in the gyration plane $\mathbf{u}_{\text{bulk,drift}}$, and the bulk velocity perpendicular to the gyration plane $\mathbf{u}_{\text{bulk},\parallel}$. The results describe average properties of the plasma environment that are applicable in a region between the solar wind-dominated environment far upstream of the comet, and the plasma environment in the direct vicinity of the nucleus. The clear ring distributions indicate that the fields affecting the cometary pickup ions are sufficiently homogeneous over this spatial scale. After dividing the observations in two groups based on the occurrence of ions with energies $> 200\,\text{eV}$ (high and low energy range observations), we find that the mean of $u_\perp$ and $\mathbf{u}_{\text{bulk,drift}}$ increase for the high energy observations, while that of $\mathbf{u}_{\text{bulk},\parallel}$ does not. This indicates that the additional energy is only distributed in the gyration plane, not in the component along the magnetic field.

Based on the gyroradii estimates (average: 340 km), we expect this region to be a few hundreds of km in size. There is a large discrepancy between the expected gyroradius of water-group pickup ion in the undisturbed solar wind ($\approx 10\,000\,\text{km}$) and the value found here. The comet plasma cloud partially shields the inner part of the coma from the solar electric field. This lower electric field strength, in combination with the increased magnetic field due to pile-up closer to the nucleus, results in much smaller ion gyroradii.

We furthermore estimate the electric field at the comet based on this homogeneous-field assumption. The resulting electric field is mostly directed anti-sunward. The average strength is $0.21\,\text{mV/m}$, and increases from $0.16\,\text{mV/m}$ to $0.24\,\text{mV/m}$ when splitting the observations in a low and high energy range. The anti-sunward component $(-E_x)$ increases for the high energy observations, while the perpendicular component (E_y) remains the same. The larger gyroradii associated with the high energy observations could indicate that the homogeneous-field assumption breaks down for the ions born furthest away from the observation point. In this scenario, the electric field is still directed anti-sunward further away from the nucleus, but less shielded by the cometary plasma cloud. The strength is therefore higher.

Another estimate for the average electric field direction is available from the solar wind proton distributions (see Moeslinger et al., 2023). Because of the larger velocities and therefore larger gyroradii, these estimates are representative of an even larger spatial scale in the upstream region of the nucleus. The fields close to the nucleus are not expected to have a significant impact on this estimate. The direction of this electric field is roughly perpendicular to the anti-sunward field close to the nucleus presented here (not shown). This is in agreement with the expected convective electric field of the upstream solar wind in the comet reference frame. The effects of the transition region between these two fields should be analysed more carefully, e. g. using simulations, in a future study. Furthermore, we mainly used the shape of the velocity distribution to estimate the electric fields in this paper. Nilsson et al. (2018) also provided another way to estimate the electric field strength by relating the measured flux of particles with their energy as a proxy for their origin. Using the results of this paper, we can also backtrace the observed particles to the approximate location of where they were ionised. Combining both approaches in a future study would help to refine the electric field measurements, and refine the validity of the homogeneous-field assumption.

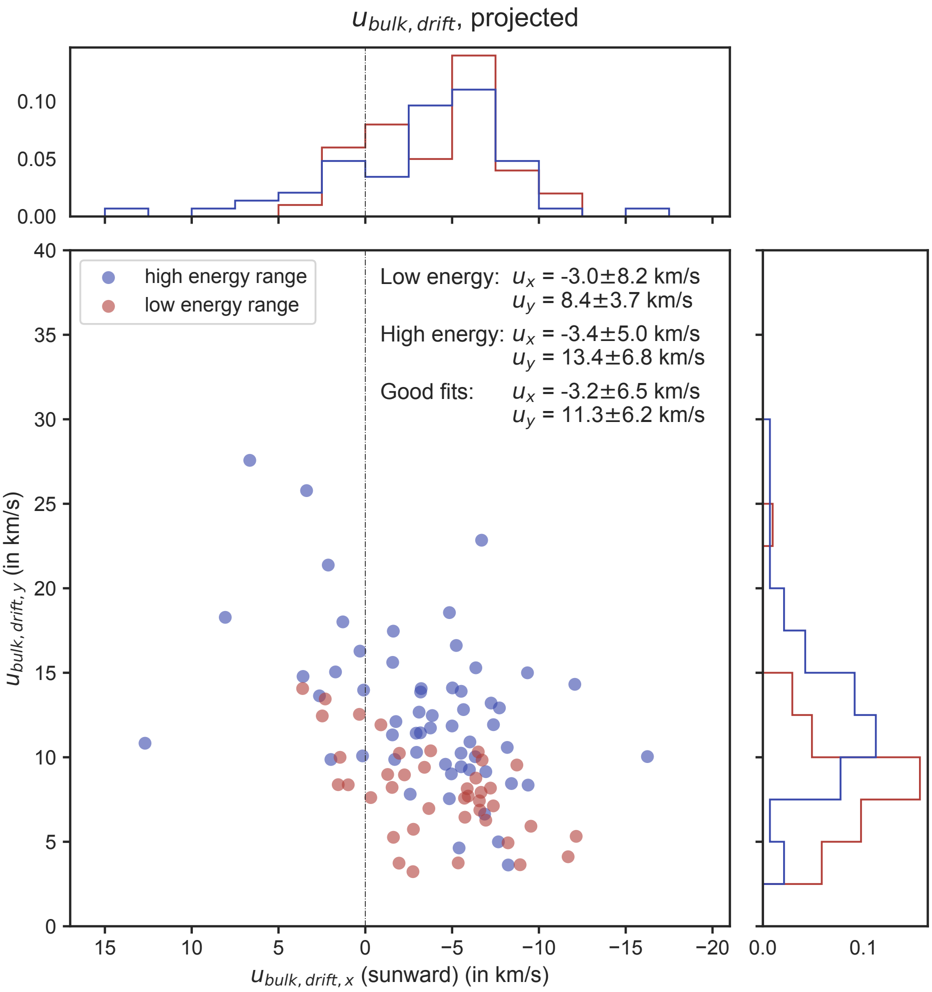

Figure A1. Scatter plot of the fitted drift velocity $\mathbf{u}_{\mathrm{bulk,drift}}$, projected into the same cartesian coordinate system as Figures 2 and 4. In this coordinate system, the z-component is always 0.

536 ## Appendix A Direction of $\mathbf{u}_{\mathrm{bulk,drift}}$

Figure A1 shows the direction of the fitted drift velocity $\mathbf{u}_{\mathrm{bulk,drift}}$ of all successful fits. The individual scans are projected into the cartesian coordinate system as described in Section 3.2. The average velocity is $[-3.2, 11.3, 0]$ km/s for good fits, so the dominant component is along the y-axis. In agreement with the electric field estimates (Figure 4), the average value of the y-component increases for the high energy scans, compared to the low energy scans. There is no significant difference found in the x-component of the same data.

Appendix B Data Availability Statement

The data used in this study is available through the ESA Planetary Science Archive (ESA PSA) and NASA Planetary Data System (NASA PDS). For RPC-ICA, the mass-separated dataset (Nilsson, 2021) was used. Magnetic field data (RPC-MAG) was obtained from Richter et al. (2019). Data analysis was done using NumPy version 1.20.2 (Harris et al., 2020). Figures were made using Matplotlib (Caswell et al., 2021; Hunter, 2007) and Colorspacious (Smith, 2015).

Acknowledgments

Rosetta is a European Space Agency (ESA) mission with contributions from its member states and the National Aeronautics and Space Administration (NASA). Work at the Swedish Institute of Space Physics in Kiruna (IRF) was funded by the Swedish National Space Agency (SNSA) grant 132/19. Work at Umeå university was supported by the SNSA grant 108/18.

References

Berčič, L., Behar, E., Nilsson, H., Nicolaou, G., Wieser, G. S., Wieser, M., & Goetz, C. (2018, 5). Cometary ion dynamics observed in the close vicinity of comet 67p/churyumov-gerasimenko during the intermediate activity period. *Astronomy and Astrophysics*, *613*. doi: 10.1051/0004-6361/201732082

Beth, A., Galand, M., Nilsson, H., Goldstein, R., Mokashi, P., Eriksson, A., … Allen, T. (2019, 9). *RPC User Guide Version 3.* Retrieved from `https://cosmos.esa.int/web/psa/rosetta`

Bieler, A., Altwegg, K., Balsiger, H., Berthelier, J. J., Calmonte, U., Combi, M., … Wurz, P. (2015, 11). Comparison of 3d kinetic and hydrodynamic models to rosina-cops measurements of the neutral coma of 67p/churyumov-gerasimenko. *Astronomy and Astrophysics*, *583*. doi: 10.1051/0004-6361/201526178

Carr, C., Cupido, E., Lee, C. G. Y., Balogh, A., Beek, T., Burch, J. L., … Trotignon, J. G. (2007). Rpc: The rosetta plasma consortium. *Space Science Reviews*, *128*(1), 629–647. Retrieved from `https://doi.org/10.1007/s11214-006-9136-4` doi: 10.1007/s11214-006-9136-4

Caswell, T. A., Lee, M. D. A., de Andrade, E. S., Hunter, J., Hoffmann, T., Firing, E., … Ivanov, P. (2021). *matplotlib/matplotlib: REL: v3.4.1* [software]. Retrieved from `https://github.com/matplotlib/matplotlib/tree/v3.4.1` doi: 10.5281/zenodo.4649959

Coates, A. J., Johnstone, A. D., Wilken, B., Jockers, K., & Glassmeier, K.-H. (1989, 8). Velocity space diffusion of pickup ions from the water group at comet halley. *Journal of Geophysical Research: Space Physics*, *94*, 9983-9993. doi: 10.1029/ja094ia08p09983

Filacchione, G., Groussin, O., Herny, C., Kappel, D., Mottola, S., Oklay, N., … Raponi, A. (2019, 1). *Comet 67p/cg nucleus composition and comparison to other comets* (Vol. 215). Springer Netherlands. doi: 10.1007/s11214-019-0580-3

Galand, M., Héritier, K. L., Odelstad, E., Henri, P., Broiles, T. W., Allen, A. J., … Wurz, P. (2016). Ionospheric plasma of comet 67p probed by rosetta at 3 au from the sun. *Monthly Notices of the Royal Astronomical Society*, *462*, S331-S351. doi: 10.1093/mnras/stw2891

Glassmeier, K., Neubauer, F., Acuna, M., & Mariani, F. (1987). Low-frequency magnetic field fluctuations in comet P/Halley's magnetosheath: Giotto observations. *Astronomy & Astrophysics*.

Glassmeier, K.-H., Boehnhardt, H., Koschny, D., Kührt, E., & Richter, I. (2007). The Rosetta Mission: Flying Towards the Origin of the Solar System. *Space Science Reviews*, *128*(1-4), 1-21. Retrieved from `http://dx.doi.org/10.1007/s11214-006-9140-8` doi: 10.1007/s11214-006-9140-8

Glassmeier, K.-H., Richter, I., Diedrich, A., Musmann, G., Auster, U., Motschmann, U., … others (2007). Rpc-mag the fluxgate magnetometer in the rosetta plasma consortium. *Space Science Reviews*, *128*(1), 649–670.

Goetz, C., Behar, E., Beth, A., Bodewits, D., Bromley, S., Burch, J., ... Volwerk, M. (2022, 12). The plasma environment of comet 67p/churyumov-gerasimenko. *Space Science Reviews*, *218*. doi: 10.1007/s11214-022-00931-1

Goetz, C., Volwerk, M., Richter, I., & Glassmeier, K. H. (2017, 7). Evolution of the magnetic field at comet 67p/churyumov-gerasimenko. *Monthly Notices of the Royal Astronomical Society*, *469*, S268-S275. doi: 10.1093/mnras/stx1570

Gunell, H., & Goetz, C. (2023). Particle-in-cell modelling of comet 67p/churyumov-gerasimenko spatial structures of densities and electric fields. *Astronomy & Astrophysics*, *674*, A65. doi: 10.1051/0004-6361/202245197

Harris, C. R., Millman, K. J., van der Walt, S. J., Gommers, R., Virtanen, P., Cournapeau, D., ... Oliphant, T. E. (2020, September). Array programming with NumPy. *Nature*, *585*(7825), 357–362. Retrieved from `https://doi.org/10.1038/s41586-020-2649-2` doi: 10.1038/s41586-020-2649-2

Hunter, J. D. (2007). Matplotlib: A 2d graphics environment. *Computing in Science & Engineering*, *9*(3), 90–95. doi: 10.1109/MCSE.2007.55

Moeslinger, A., Wieser, G. S., Nilsson, H., Gunell, H., Williamson, H. N., LLera, K., ... Richter, I. (2023, 2). Solar wind protons forming partial ring distributions at comet 67p. *Journal of Geophysical Research: Space Physics*, *128*. doi: 10.1029/2022JA031082

Neugebauer, M., Lazarus, A., Balsiger, H., Fuselier, S., Neubauer, F., & Rosenbauer, H. (1989). The velocity distributions of cometary protons picked up by the solar wind. *Journal of Geophysical Research: Space Physics*, *94*(A5), 5227-5239. Retrieved from `https://agupubs.onlinelibrary.wiley.com/doi/abs/10.1029/JA094iA05p05227` doi: https://doi.org/10.1029/JA094iA05p05227

Nilsson, H. (2021). *ROSETTA-ORBITER 67P RPCICA 4 EXT2 RESAMPLED AND CALIBRATED V1.0* [dataset]. ESA Planetary Science Archive and NASA Planetary Data System. Retrieved from `https://pdssbn.astro.umd.edu/holdings/ro-c-rpcica-4-ext2-phys-mass-v1.0/dataset.shtml`

Nilsson, H., Behar, E., Burch, J. L., Carr, C. M., Eriksson, A. I., Glassmeier, K. H., ... Karlsson, T. (2021, 1). *Birth of a magnetosphere.* wiley. doi: 10.1002/9781119815624.ch27

Nilsson, H., Gunell, H., Karlsson, T., Brenning, N., Henri, P., Goetz, C., ... Vallières, X. (2018, 8). Size of a plasma cloud matters: The polarisation electric field of a small-scale comet ionosphere. *Astronomy and Astrophysics*, *616*. doi: 10.1051/0004-6361/201833199

Nilsson, H., Lundin, R., Lundin, K., Barabash, S., Borg, H., Norberg, O., ... Burch, J. L. (2007, 5). Rpc-ica: The ion composition analyzer of the rosetta plasma consortium. *Space Science Reviews*, *128*, 671-695. doi: 10.1007/s11214-006-9031-z

Nilsson, H., Williamson, H. N., Bergman, S., Stenberg Wieser, G., Wieser, M., Behar, E., ... Goetz, C. (2020, 09). Average cometary ion flow pattern in the vicinity of comet 67P from moment data. *Monthly Notices of the Royal Astronomical Society*, *498*(4), 5263-5272. Retrieved from `https://doi.org/10.1093/mnras/staa2613` doi: 10.1093/mnras/staa2613

Reinhard, R. (1987, jun). The giotto mission to comet halley. *Journal of Physics E: Scientific Instruments*, *20*(6), 700–712. Retrieved from `https://doi.org/10.1088/0022-3735/20/6/029` doi: 10.1088/0022-3735/20/6/029

Richter, I., Glassmeier, K.-H., Goetz, C., Koenders, C., Eichelberger, H., & Cupido, E. (2019). *ROSETTA-ORBITER 67P RPCMAG 3 EXT2 CALIBRATED V9.0* [dataset]. ESA Planetary Science Archive and NASA Planetary Data System. Retrieved from `https://pdssbn.astro.umd.edu/holdings/ro-c-rpcmag-3-ext2-calibrated-v9.0/dataset.shtml`

Smith, N. J. (2015). *Colorspacious* [software]. Retrieved from `https://colorspacious.readthedocs.io/en/latest/overview.html` doi: 10.5281/zenodo.1214904

Vigren, E., & Eriksson, A. I. (2019, 1). On the ion-neutral coupling in cometary comae. *Monthly Notices of the Royal Astronomical Society*, *482*, 1937-1941. doi: 10.1093/mnras/sty2869

Williamson, H. N., Nilsson, H., Stenberg Wieser, G., A. Moeslinger, A., & Goetz, C. (2022, 4). Development of a cometosheath at comet 67p/churyumov-gerasimenko a case study comparison of rosetta observations. *A&A*, *660*. Retrieved from `https://doi.org/10.1051/0004-6361/202142461` doi: 10.1051/0004-6361/202142461

Indirect Observations of Electric Fields at Comet 67P

A. Moeslinger[1,2], H. Nilsson[1,2], G. Stenberg Wieser[1], H. Gunell[2], C. Goetz[3]

[1]Swedish Institute of Space Physics, 981 28 Kiruna, Sweden
[2]Department of Physics, Umeå University, 901 87 Umeå, Sweden
[3]Department of Mathematics, Physics and Electrical Engineering, Northumbria University, Newcastle-upon-Tyne, United Kingdom

Key Points:

- Rosetta observations show partial ring distributions of cometary ions at comet 67P.
- From the velocity distributions the plasma bulk velocity and gyration speed are determined.
- We estimate the electric field from the bulk velocity and find a mostly anti-sunward field of 0.21 mV/m.

Corresponding author: A. Moeslinger, `anja.moeslinger@irf.se`

Abstract

No spacecraft visiting a comet has been equipped with instruments to directly measure the static electric field. However, the electric field can occasionally be estimated indirectly by observing its effects on the ion velocity distribution. We present such observations made by the Rosetta spacecraft on 19th of April 2016 when comet 67P was at a low outgassing rate and the plasma environment was relatively homogeneous. The ion velocity distributions show the cometary ions on the first half of their gyration. We estimate the bulk drift velocity and the gyration speed from the distributions. By using the local measured magnetic field and assuming an $\mathbf{E} \times \mathbf{B}$ drift of the gyrocentre, we get an estimate for the average electric field driving this ion motion. We analyse a period of 13 h, during which the plasma environment does not change drastically. We find that the average strength of the electric field is 0.21 mV/m. The direction of the electric field is mostly anti-sunward. This is in agreement with previous results based on different methods.

Plain Language Summary

Measuring the static electric field in space plasmas is difficult. Most spacecraft do not have dedicated instruments for it, and the Rosetta mission to comet 67P is no exception. But the electric field is one of the main governing factors behind for the motion of newly born cometary ions. In this study, we use measurements of the cometary ions to estimate the average electric field close to the nucleus. The observations are made on the 19th of April 2016 by the Ion Composition Analyzer (ICA), which measures the energy and travel direction of the different plasma species. The specific shape of the observed velocity distribution of cometary ions – a partial ring – indicates that the fields accelerating the observed cometary ions are relatively homogeneous. The spatial scale this applies to is approximately one gyroradius, which we estimated to be around 340 km. The resulting electric field is 0.21 mV/m, which is significantly smaller than the expected field in the upstream solar wind, far away from the nucleus.

1 Introduction

The atmospheres of comets are produced by the sublimation of ice near the nucleus' surface. During this sublimation, the ice (primarily water and CO_2) also lifts off dust from the nucleus surface. Cometary dust is usually comprised of organic and rocky material (Filacchione et al., 2019). The intensity of this process is quantified as the outgassing or production rate. It is modulated by the strength of the solar irradiation at the comet's position, and depends on the size and composition of the comet itself. The outgassing rate therefore varies along the comet's elliptical trajectory, and even more so between different comets. Due to the low mass of the comet nucleus (in comparison to e. g. planets) the atmosphere is gravitationally unbound and expands freely into space (Bieler et al., 2015). Some of the molecules in this atmosphere become ionised by EUV flux or electron-impact-ionisation and form a plasma cloud of newborn cometary ions (Galand et al., 2016). The newborn ions are accelerated by the electromagnetic fields around the nucleus. These fields are the result of the interaction between the solar wind and the cometary plasma cloud (Nilsson et al., 2021).

In the comet reference frame the solar wind travels with a speed of around 400 km/s in the anti-sunward direction. In combination with the frozen-in magnetic field this creates a convective electric field at the comet. Newborn ions are accelerated in direction of the electric field in a process often referred to as ion pick-up. The accelerated ions are called pick-up ions. They gyrate due to the magnetic field and gain energy due to the electric field. The relative size of the plasma environment can be characterised by comparing it to the gyroradius of the ions. If the plasma environment is much larger than the ion gyroradius, fluid dynamics is appropriate to describe the main physical processes, as in the example of comet 1P/Halley. Once the plasma environment is of a similar spatial scale as the ion gyroradius, kinetic effects have to be taken into account. This is the case for comet 67P, especially at a low outgassing rate far away from the Sun (Goetz et al., 2022).

Under typical solar wind conditions, the gyroradius of cometary water ions is on the order of ten thousand kilometres. If the spatial scale of the plasma interaction region between the solar wind and the comet is much larger than this gyroradius, the pick-up ions form ring distributions in velocity space. Such distributions were observed during the fly-by of the Giotto spacecraft at comet 1P/Halley (Reinhard, 1987). By pitch-angle scattering these rings can evolve into shell distributions. The gyrocentre of the distributions is the solar wind velocity component perpendicular to the magnetic field (Coates et al., 1989). The ring and shell distributions were observed essentially everywhere in the coma of 1P/Halley, from 5 million kilometres away from the nucleus to the the bow shock (Neugebauer et al., 1989). Additionally, enhancements in the power spectra of the magnetic field at the water ion cyclotron frequency were observed (K. Glassmeier et al., 1987). This is the same frequency the water ions gyrate with when forming ring and shell distributions.

A very different situation is present at comet 67P/Churyumov-Gerasimenko (hereafter: comet 67P), target of the Rosetta mission (K.-H. Glassmeier, Boehnhardt, et al., 2007). The outgassing rate of comet 67P is much lower than 1P/Halley, even at perihelion. As a consequence, the spatial scales of the plasma environment are also much smaller. Because the Rosetta spacecraft was usually orbiting the comet at walking speed relatively close to the nucleus, the nature of the observations are very different compared to Giotto observations. The observations in the terminator plane probe the plasma environment of the newborn cometary pickup ions. The evolution to full ring and shell distributions is expected to happen much further downstream, in the tail of comet 67P (Williamson et al., 2022).

Estimating the gyroradius close to the nucleus is difficult, as it requires knowledge about the electric field. Previously, estimations of the electric field direction were based on the assumption that the ions are unmagnetised, and are therefore accelerated and flowing along the electric field (Nilsson et al., 2018). This method only gives the direction of the field, not it's strength. If the ion gyroradii are very large, the assumption of unmagnetised ions holds. The ions are observed as uni-directional. Rosetta has no dedicated instruments that are capable of measuring the static electric field with sufficient accuracy. However, the velocity distribution of cometary pick-up ions gives us information about the plasma environment close to the nucleus. If we observe the beginning of a gyration in the velocity distribution of cometary ions we can characterise the electric field and gyroradius close to the nucleus. In this paper, we present observations of partial ring distributions in the cometary pick-up ion data, and show how they relate to the electric fields around the comet.

2 Instrument Description

To derive the ion velocity distributions of the cometary plasma environment, we use data from the Ion Composition Analyzer (ICA), part of the Rosetta Plasma Consortium (RPC; Carr et al., 2007). In addition to that, we use magnetic field measurements from the magnetometer MAG, also part of the RPC instrument package. Both instruments are described below. More information about RPC can be found in the RPC User Guide (Beth et al., 2019).

2.1 Ion Composition Analyzer

ICA was designed to measure the velocity distributions of the major positive ion species around comet 67P (Nilsson et al., 2007). The mass resolution of the instrument allows us to distinguish between protons (H^+), alpha particles (He^{2+}), He^+, and heavier ions, such as H_2O^+ and CO_2^+. The energy range covers low energy ions at a few eV/q up to energies of 40 keV/q. There are 96 energy bins in total, which are logarithmically spaced.

The nominal instrument field-of-view is $360° \times 90°$ (azimuth × elevation). This angular field-of-view is subdivided in 16 azimuth and 16 elevation angles. An individual pixel in this 16×16 grid has therefore a nominal size of $22.5° \times 5.625°$. All 16 azimuth directions are measured simultaneously. The different elevations are measured in sequence. The full energy range is measured for each elevation. A full measurement cycle covering all elevations and energies, also referred to as "scan", takes 192 s. Due to the limited resolution of the instrument's high voltage supply the elevation angles at low energies (up to approximately 100 eV/q) depend on the measured energy. This results in a changing pixel boresight at different energies. To compensate for this effect, we resample the elevation angles of each azimuth sector into 17 equally-spaced angles that cover the nominal 90° elevation. Parts of the ICA field-of-view are obstructed by the spacecraft and solar array, but this is not expected to affect the results shown here. In this study we use the L4-PHYSMASS dataset, which contains differential flux for H^+, He^{2+}, and heavier ions.

2.2 Magnetometer

The magnetometer MAG consists of two triaxial fluxgate magnetometers that are mounted on a spacecraft boom. The measurement range is ±16 384 nT in each direction, with a resolution of 20 bit (31 pT). The vectors are sampled with a frequency of 20 Hz (K.-H. Glassmeier, Richter, et al., 2007). For the purpose of this study, we average the magnetic field data over the duration of one ICA scan, which eliminates high-frequency disturbances. There is a remaining unknown offset in the data due to temperature drifts of the instrument. This offset is of the order of a few nT for each axis, and can affect the magnitude and direction estimate of the magnetic field. With a typical measured magnetic field strength of 20 nT the error is expected to be below 15° for the time period considered in this study.

3 Methods

The starting point for our analysis is the velocity distribution of cometary pickup ions. To quantify and interpret them we apply a ring fitting procedure to the observed energetic cometary ion population. The resulting fitted velocities are projected into a coordinate system that is decoupled from changes in the plasma environment (e. g. a change in magnetic field direction) for better comparison between the individual scans. From the fitted velocities we can derive an estimate for the average electric field.

3.1 Ring Fitting

As we will show in section 4, there is an energy-angle dispersion in the distribution of cometary ions. We use a ring fitting procedure to estimate the bulk flow properties of the energetic cometary plasma. This procedure is presented in Moeslinger et al. (2023), but in this study we apply it to the dataset of cometary pickup ions. We will outline the main algorithm and its limitations below.

In a first step, we estimate the plane that contains the data. This plane corresponds to the gyration plane of the particles, which is perpendicular to the estimated magnetic field direction. From this step we get the parallel (to the magnetic field) bulk flow velocity $\mathbf{u}_{\text{bulk},\parallel}$. Normalising this vector gives the unit vector $\mathbf{r}_{\text{bulk},\parallel}$, which is the plane normal. In the second step we fit a sphere to the data, with the constraint that the centre of the sphere must lie on the plane determined in the first step. The intersection of both results gives a circle with a radius that corresponds to the gyration velocity $u_\perp$. The offset between the fitted centre of the sphere and $\mathbf{u}_{\text{bulk},\parallel}$ is the drift velocity of the bulk plasma $\mathbf{u}_{\text{bulk,drift}}$. In both steps we use a weighted non-linear least squares fitting algorithm. More information can be found in Moeslinger et al. (2023). The fitting is done individually for each ICA scan. The velocity vectors used for fitting are the median energy vectors of the cometary ions for each azimuth/elevation pixel. As we are interested in the pickup ion population, the energy bins below 40 eV are excluded from the analysis. These low energy ions typically belong to a different ion population with a different flow direction (see Berčič et al., 2018; Nilsson et al., 2020). We also discard pixels with zero flux. The median energy is defined as the energy bin where the flux integrated in energy from 40 eV up to this bin exceeds 50 % of the total flux of the pixel. This median energy is converted to velocity vectors assuming a water ion plasma. The logarithm of the total flux for each vector is used as a weight parameter for the fitting procedure.

3.2 Projections

The fitted velocity parameters obtained by the the algorithm in Section 3.1 are in ICA instrument coordinates. Due to the low spacecraft velocity with respect to the comet (of the order of a few m/s) this is essentially the rest frame of the comet nucleus. However, the alignment of the instrument coordinate system is arbitrary with respect to the plasma flow. Therefore, we define a new coordinate system, which is determined individually for each scan. In this system:

1. The z-axis is aligned with the direction of $\mathbf{u}_{\text{bulk},\parallel}$. This reduces the gyration to the x-y plane. To ensure a consistent gyration direction for all scans, the sign is determined by the local magnetic field (i. e., $\hat{\mathbf{z}} \cdot \mathbf{B} > 0$).
2. The x-axis is the sunward direction, projected onto the gyration plane.
3. The y-axis completes the right-handed system.

This coordinate system decouples the observed ion distribution from changes in the plasma environment, such as the magnetic field direction. The resulting fitted velocities can be compared in both magnitude and direction over longer timescales. It also allows for an easier analysis of the velocity distributions and the accuracy of the fitting procedure. For this purpose, we project the measured data into a cartesian velocity grid, converting them to velocity vectors assuming a mass per charge of 18 amu/q (single charged water ions) as above. In this reference frame, the x-y projection contains the velocity distribution information that shows the gyration pattern of the ions.

3.3 Electric Field

The drift velocity in the gyration plane determined from the ring fits, $\mathbf{u}_{\text{bulk,drift}}$, is the result of electric fields around the comet. If we assume that the electric and magnetic fields are homogeneous over the relevant spatial scales, the drift velocity is given by:

$$\mathbf{u}_{\text{bulk,drift}} = \frac{\mathbf{E} \times \mathbf{B}}{B^2} \qquad \Rightarrow \qquad \mathbf{E} = -\mathbf{u}_{\text{bulk,drift}} \times \mathbf{B} \tag{1}$$

To fully utilise the information obtained by the ring fitting procedure, we only use the z-component of the measured local magnetic field vector. This is the component along the estimated parallel bulk flow of the cometary plasma, and the estimated electric field is confined to the gyration plane.

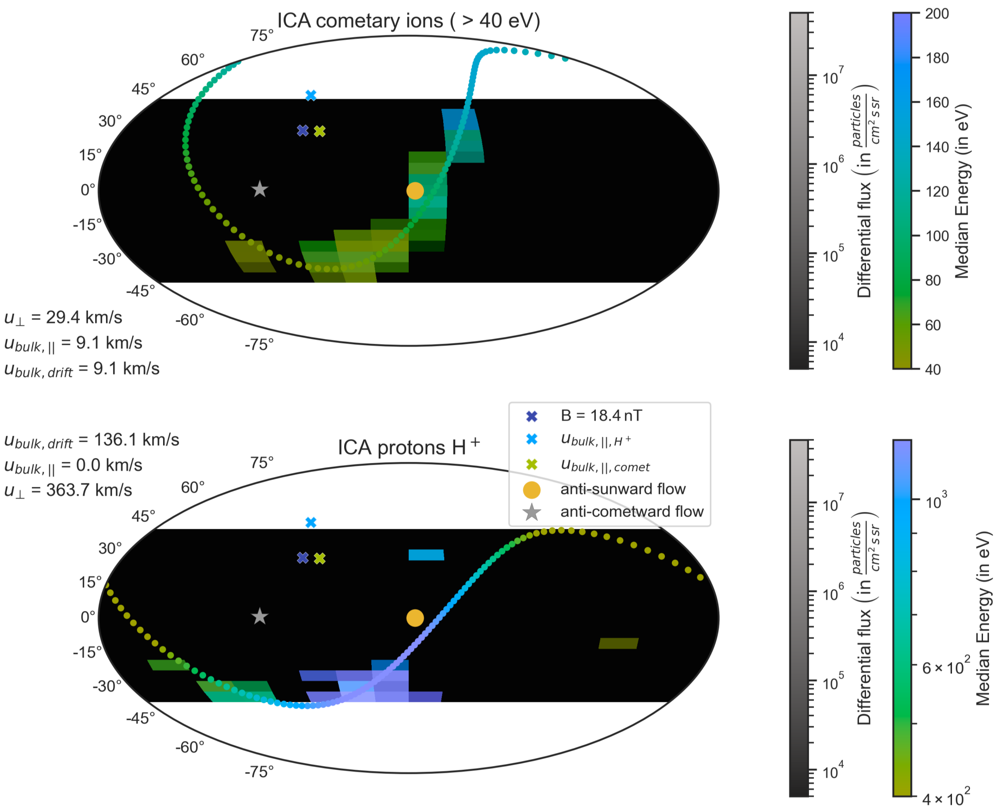

Figure 1. Dual colourmap plots of the cometary ions (top panel) and the solar wind protons (bottom panel). The background shows one ICA scan, taken at 06:38:24. No particle flux was detected for the black pixels. The white areas are not covered by the ICA field-of-view. The dots in both panels show the result of the ring fitting procedure for each species. For more information see text..

4 Results

We present results from a case study using data from April 19th, 2016, when comet 67P was at a heliocentric distance of 2.8 AU. Only the time period between 00:00 - 13:00 is included. This is the same time period as analysed in Moeslinger et al. (2023). The rest of the day exhibits strong fluctuations in the magnetic field as well as spacecraft manoeuvres and is therefore not suitable for studying partial ring distributions.

4.1 Velocity Distributions of Cometary Ions

Any distribution with a large angular spread may partially fall outside the field-of-view of the instrument. To monitor these limitations, we assess the measured velocity distributions directly in instrument coordinates, as shown in Figure 1. The upper panel shows the cometary ions with energies above 40 eV. Protons are shown in the lower panel. The plots visualise the median energy as the hue of each pixel, and the differential flux, integrated over the entire energy range considered, as its intensity. More information on this visualisation method and a discussion of the solar wind protons can be found in Moeslinger et al. (2023).

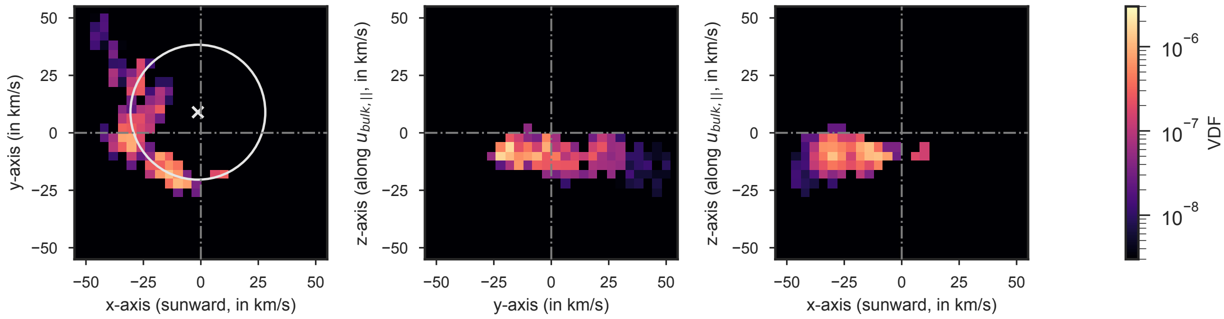

Figure 2. Projected velocity distributions of the cometary ions. The data is the same as shown in Figure 1, but converted to velocity and projected into a cartesian coordinate system. The colourbar shows the velocity distribution function (VDF) of each bin. The z-axis is aligned with the estimated parallel direction ($u_{\text{bulk},\|}$) and oriented almost parallel to the local measured magnetic field. The x-axis is the component of the sunward direction perpendicular to the z-axis, and the y-axis completes the right-handed system.

Figure 1 shows a typical example of the distributions of cometary and solar wind ions during one ICA scan. ICA does not cover elevations exceeding ±45° (white areas). The energy-angle dispersion is clearly visible in both populations. In case of the cometary ions, the highest observed median energies are around 150 eV. The results of the ring fitting procedure are indicated by the dots, colour-coded with the respective energy colour scale. The estimated normal vector of the gyration plane is indicated by the green (cometary ions) and light blue (protons) cross. The dark blue marker shows the magnetic field direction. Both normal vector estimates are within 15° of the local magnetic field measurement. The fitted velocities for the cometary ions are $u_{\text{bulk,drift}} = 9.1\,\text{km/s}$, $u_\perp = 29.4\,\text{km/s}$, and $u_{\text{bulk},\|} = 9.1\,\text{km/s}$.

A different perspective of the same data is given in Figure 2. The measurements of each pixel were converted to velocities in a cartesian coordinate system, as described in Section 3. The three panels show the projections on the x-y, y-z, and x-z plane. The data is integrated over the third dimension. In panel a) the fitted ring and its centre, the estimated bulk drift velocity, are indicated. The fitted ring is a good approximation of the measured data. The lowest velocities in the gyration plane are about 20 km/s, which corresponds to the lower energy threshold at 40 eV. These low velocities are found in the direction opposite of the drift velocity. The maximum velocities are at around 40 km/s. These ions have completed a little less than half a gyration compared to the lowest energy ions. As there is no complete ring distribution, all observed ions are expected to be on their first gyration. The “side views” of the data, shown in panels b) and c), are quite flat and only spread horizontally. This indicates that the data is indeed mostly distributed on a plane, and the $\mathbf{r}_{\text{bulk},\|}$ estimate is a good estimator of the plane. The parallel velocity component varies a few km/s around the fitted value of 9.1 km/s.

The data analysis shown in Figures 1 and 2 was done for a 13 h time period, from 00:00 - 13:00 on April 19th, 2016. There are a total of 225 ICA scans available during this period. A preliminary inspection of the cometary ion data as shown in Figure 1 (without the ring fitting) showed that 169 of these 225 scans are suited for a ring fitting algorithm. The scans excluded in this step either have too little data (e. g. only a few pixels contain any flux), or there is no clear energy-angle dispersion visible. The ring fit-

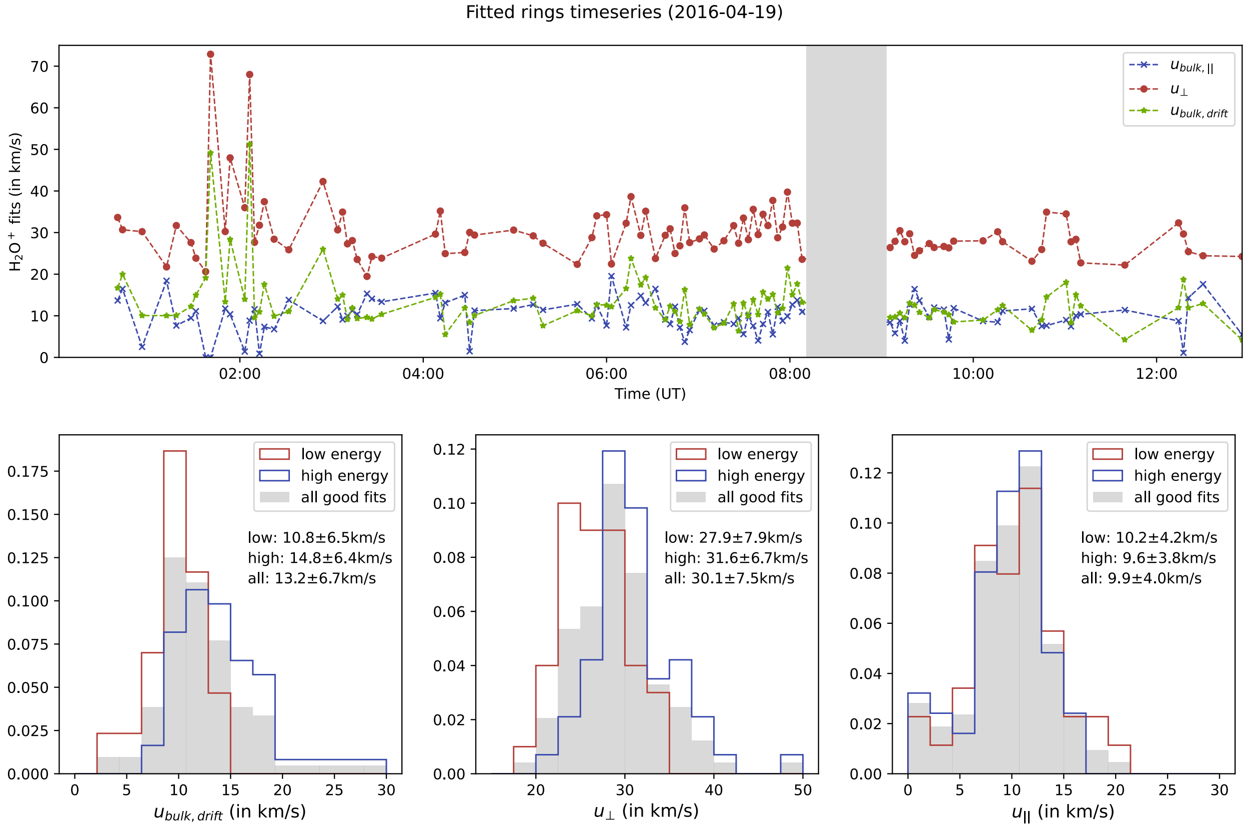

Figure 3. Resulting fitted velocities for 2016-04-19, from 00:00 – 13:00. Top row: timeseries of the three fitted velocities for cometary ions. Only the 99 good fits are included. No ICA data is available for the time indicated by the grey areas. Bottom row: histograms of the distribution of the fitted velocities for the same data as the top row. The left panel shows the bulk drift velocity. The middle panel shows the fitted gyration velocity $u_\perp$. The right panel shows the parallel velocity. The grey histograms show the distribution of all good fits. The red and blue histograms show the distributions of the good fits separated in scans with low and high energy range; see text for more details. All histograms are normalised. The y-axes are corresponding densities (arbitrary units). The text insets give the mean and standard deviation for each distribution.

ting algorithm yielded a successful fit in 99 of these 169 scans, based on visual inspection. The criteria for a successful fit include good agreement between data and fit in both angular space as well as energy. To analyse why the success rate was not higher, we performed a principal component analysis (PCA) of the underlying data. We found that the fitting algorithm works better for larger PCA variances (data not shown). We interpret this as a requirement for sufficient spread of the data points to give stability to the fitting procedure. If the points are distributed mostly along a straight line in 3D space, the plane this line lies on is not well defined. Only if the line deviates significantly from a straight line, as in the case of a partial ring with sufficient angular extent, the plane is well-defined. In this case, both the first and the second PCA component variance are sufficiently large. In the case of good fits, the third PCA vector aligned very well with the corresponding parallel vector estimate from the ring fitting procedure.

A timeseries of the resulting velocities can be seen in figure 3, top panel. The plot only includes good fits. The dominating velocity is the gyration speed $u_\perp$, with an average of 30.1 km/s. The magnitude of the bulk drift velocity is about half of the gyration speed. The average is 13.2 km/s. $u_{\mathrm{bulk,drift}}$ and $u_\perp$ are correlated. The parallel bulk velocity is usually the smallest of the three (average: 9.9 km/s), and does not correlate with the other two.

The statistical distribution of the three fitted velocity components can be seen in the bottom row of Figure 3. The grey histograms show the normalised distribution of all good fits for each velocity component. The distributions of $u_{\mathrm{bulk,drift}}$ and $u_\perp$ are roughly gaussian-shaped, with slightly elongated tails towards higher velocities. The standard deviations of the distributions are very similar, with 6.7 km/s and 7.5 km/s for $u_{\mathrm{bulk,drift}}$ and $u_\perp$, respectively. The distribution of $u_{\mathrm{bulk},\|}$ does not have a high velocity tail. Instead, there is a slight increase for very low velocities. This is because the fitting procedure effectively gives the absolute value of the parallel component. Any negative values in a fixed frame (e. g. B-field aligned) are mapped onto their positive counterparts, creating this artificial peak at velocities close to zero.

Inspecting all individual gyration patterns (as shown in Figure 2) we noticed a change when the maximum energy observed is higher. Therefore, we divided the good fits into two categories: “high energy” and “low energy” scans. The “high energy” scans contain pixels where the median energy exceeds 200 eV. This is the case for 58 out of the 99 good fits, for the remaining 41 scans the median energy of every pixel is below 200 eV. Both $u_{\mathrm{bulk,drift}}$ and $u_\perp$ have the distribution shifted towards higher velocities for the high energy scans, compared to the low energy scans. The distribution of $u_\|$ on the other hand appears almost identical for both cases.

4.2 Electric Fields

We can use the fitted drift velocity of the plasma bulk flow to get an estimate of the average electric field. The magnetic field used to calculate the electric field (according to Equation 1) is the $\mathbf{r}_{\mathrm{bulk},\|}$-aligned component of the average measured magnetic field for each scan. The results are projected into the same coordinate system used for Figure 2. This way, we can compare the scans in a statistical manner.

Figure 4 shows the electric field estimates of all good fits, split up into high energy and low energy scans. The plot shows the x-y plane, which contains all necessary information. As the magnetic field is exclusively along the z-axis in this frame the z-component of the electric field is zero. The electric field is dominated by an anti-sunward component for all scans. It ranges from -0.05 mV/m to -0.35 mV/m along E_x. The mean is -0.2 mV/m. The high energy scans show a larger E_x component, with a mean of -0.23 mV/m, compared to the low energy scans (mean: -0.15 mV/m). No such dependence on the energy range can be identified in the E_y component. It ranges from 0.05 mV/m to -0.25 mV/m, with a mean of -0.06 mV/m. The distributions along E_x and E_y are also shown by the histograms on top and left of the main figure. The similarity of the high and low energy distributions for the E_y component is evident. A tendency towards stronger anti-sunward fields for high energy scans can also be identified in the E_x-histogram.

The inset on the upper left corner shows the distribution of the magnetic field strength used for calculating the electric field. Overall, the distributions for the high and low energy cases are very similar. There is no favour towards higher magnetic fields for the high energy cases that could influence the results of the electric field estimate. The second inset shows the magnitude of the E-field estimate. There is a tendency for higher electric field strengths for the high energy scans as well, but it is not as pronounced as for E_x.

A timeseries of the same dataset as in Figure 4 is shown in Figure 5. Until 03:00 the E-field estimates vary significantly, both between individual scans and over time. After 03:00 the variability over time becomes less. There is another clearly noticeable peak

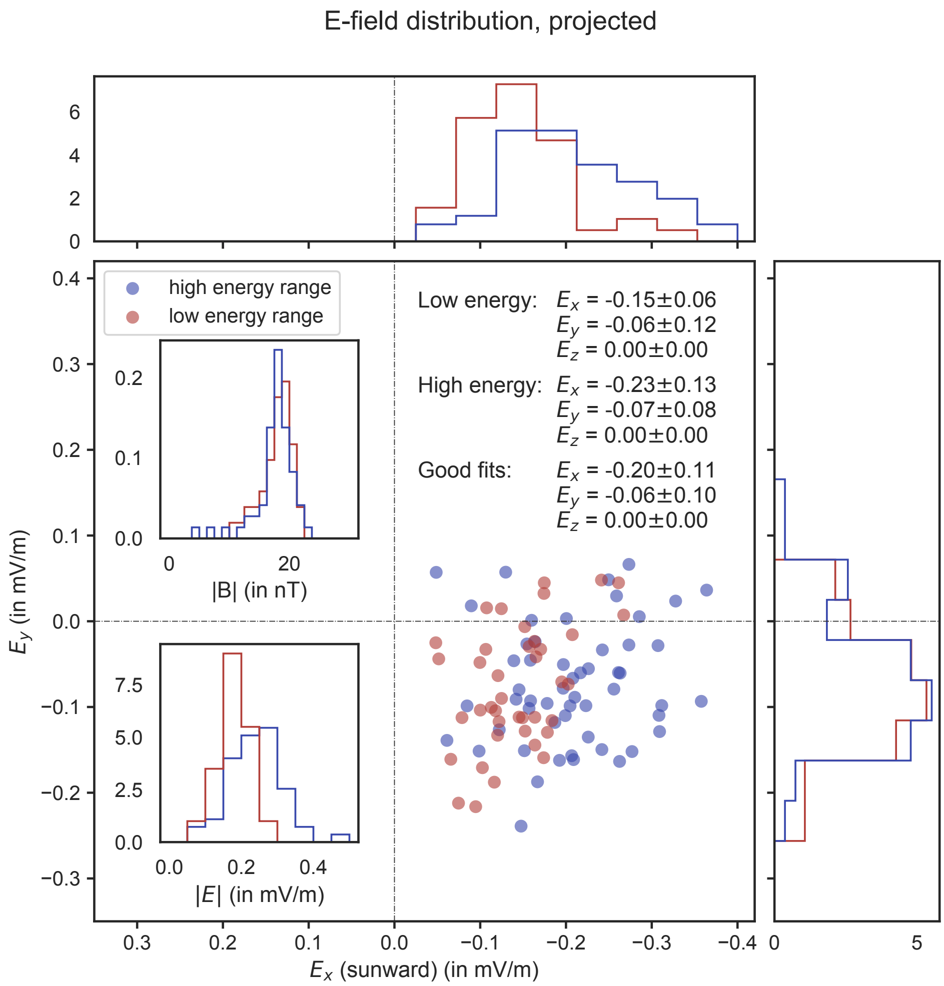

Figure 4. Distribution of the electric field estimates. Only the good fits, split up between high and low energy range scans, are included. The results are projected into the same cartesian coordinate system as used in Figure 2. The magnetic field used for the calculation of the E-field estimate is the z-component of the measured magnetic field (in this cartesian coordinate system). The inset in the upper left corner shows a histogram of the magnitude of the magnetic field. In the lower left corner another inset shows the distribution of the E-field along the z-axis. The text gives the statistical properties of the individual distributions (all values in mV/m). For more information see text.

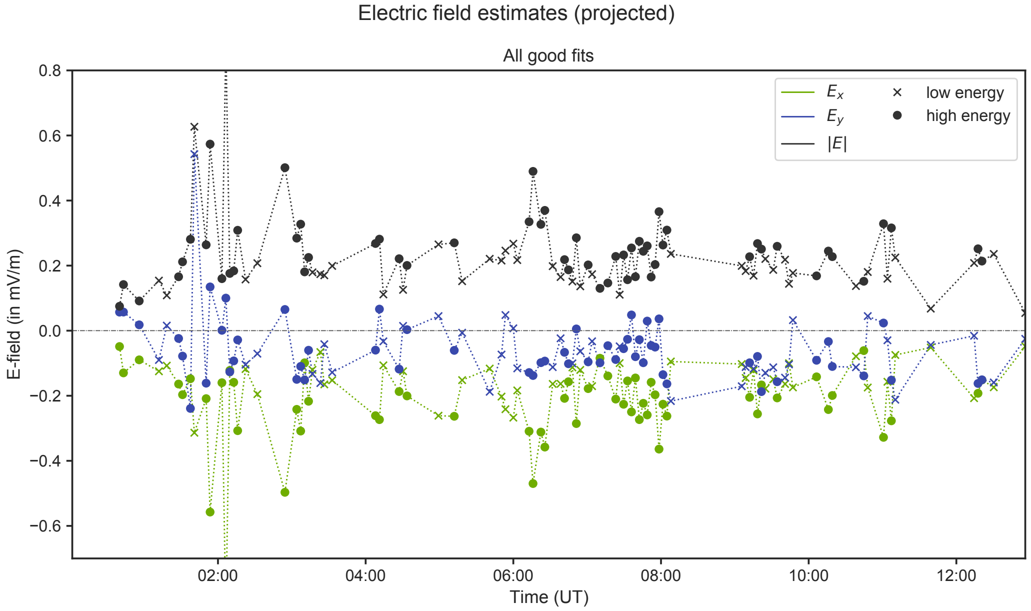

Figure 5. Timeseries of the estimated electric field. The coordinate system for the individual components is the same as used for Figures 2 and 4 (i. e., E_x is sunward in the gyration plane). The E_x and E_y components as well as the magnitude are displayed. The E_z-component is zero for all scans and therefore not shown. Different markers indicate whether the estimate belongs to a high (circle) or a low (cross) energy scan.

around 06:00. An anti-sunward electric field component (negative E_x) dominates the total electric field in almost all cases. The occurrence of high or low energy scans does not show consistent patterns over time. During some periods there are several consecutive scans of the same type, for example around 06:00, and between 07:00-08:00. After 09:00 on the other hand, the high and low energy scans alternate almost every successful fit.

5 Discussion

As shown in Figure 1 there is a clear energy-angle dispersion visible in the cometary ions above 40 eV. Such partial ring distributions can only form in a plasma environment with sufficiently homogeneous electric and magnetic fields. Of the observed particles, the most energetic ones have completed almost half a gyration, so the ions cannot be regarded as unmagnetised. However, the spatial scale of the interaction region is not large enough for the formation of fully developed rings. If the fields were heterogenous there would be more randomness in the ion velocity distribution pattern and the partial rings would be smeared out. Occasionally, some energetic ions with energies far above 200 eV occur outside of the partial ring pattern (not shown). We believe that these are born outside the homogeneous interaction region, possibly in a region that is more dominated by the solar wind given their high energies. These random high-energy ions usually interfere with the ring fitting procedure and are therefore excluded from the results.

From the fitted rings we can deduce the bulk flow of the energetic cometary plasma (see Section 5.1). The obtained fitting parameters can also be used to infer other quantities of the plasma environment. With the gyration speed $u_\perp$ we can estimate the gyroradius of the particles. The drift velocity in the gyration plane $\mathbf{u}_{\mathrm{bulk,drift}}$ gives us an estimate for the electric field strength and direction. This is discussed in further detail in Section 5.2.

5.1 Velocity Distributions

There are no significant changes in the spacecraft pointing with respect to the sunward and cometward directions during the considered time period. However, the same cannot be said for the plasma environment. Even if the fields are homogeneous, they can slowly change over time. This can easily be seen in the change of the locally measured magnetic field from scan to scan, but is equally applicable to the electric field. To quantify the changes in the plasma environment we analysed the variability of the magnetic field as well as the fitted $\hat{\mathbf{r}}_{\mathrm{bulk},\parallel}$. For each scan with a good fit we looked at the angle between the direction and the average direction over the entire observation period. The angular variability relative to the measured magnetic field is on average 18°, but even exceeds 30° in multiple cases. The variability relative to the mean in the direction of $\hat{\mathbf{r}}_{\mathrm{bulk},\parallel}$ are slightly less, with an average of 12.5° (good fits only). Deviations above 30° are possible in this case as well. A static coordinate system is therefore not suitable. Instead we used the $\hat{\mathbf{r}}_{\mathrm{bulk},\parallel}$ estimate to calculate the projection as described in Section 3.2. In this coordinate system the bulk drift velocity and electric field estimates of the individual scans can be systematically compared over the entire observation period.

In the simplest theoretical case of ion pickup in a homogeneous plasma, for example in the undisturbed solar wind, the ratio between the gyration speed and the drift speed is 1. This is a direct consequence of the ions being introduced into the system with 0 velocity. The average speed is the drift speed as determined by the background electric field, but the maximum speed of the particle is twice that. In our case the ratio $u_\perp/u_{\mathrm{bulk,drift}}$ is 2.3 for all good fits, 2.1 for the high energy scans, and 2.6 for the low energy scans. Consequently, the minimum speed of the particles gyrating along the fitted rings never reaches 0. Drift velocities of approximately 13 km/s further indicate that the observed velocity distributions are not directly caused by ion pickup in the undisturbed solar wind electric field. For this case, drift velocities of the order of 400 km/s are expected. We rather see pick-up in a region that is mostly shielded from the solar wind electric field and consequently has a lower drift speed.

An estimate for the spatial scales of the interaction region that forms the observed partial rings is the gyroradius of the cometary ions: $r_g = \frac{mu_\perp}{qB}$. The gyroradius is defined in the electric-field-free reference frame. Due to the lack of knowledge about the electric field strength it usually cannot be calculated properly at comet 67P. We get the required gyration speed $u_\perp$ directly from our fitted rings. The mass m and charge q are assumed to be 18 amu and 1.6×10^{-19} C (singly charged water ions). For the magnetic field we use the z-component of the locally measured magnetic field in the projected coordinate system. The average gyroradius for all good fits is 340 km. High energy scans have on average a larger gyroradius (364 km) than low energy scans (306 km). We therefore expect the interaction region in which the rings are formed to be somewhat larger for the case of high energy scans. These values are much smaller than the expected gyroradii in the undisturbed solar wind (approx. 10 000 km). At the same time, they are much larger than the distance between the spacecraft and the nucleus (35 km). The observed ions, especially those with higher energies that have completed more than a quarter of a gyration, must therefore originate from an area further away from the nucleus than the Rosetta spacecraft.

Apart from some large fluctuations in the beginning of the day, the variation in the magnitude of all three fitted velocities are rather small (see Figure 3). Some differences in the mean values of the individual distributions of high and low energy scans are found. No significant differences in the standard deviations of the distributions between the high energy scans and the low energy scans are found. The uncertainties in the measured energy due to the limited energy resolution of the instrument and the derived velocity estimate may contribute to this spread in the fitted velocities. The energy bin width of ICA increases with higher energies, potentially increasing the spread of the distribution when higher energies are measured. As we see no such increase from low to high energy range scans in the results, the main contributing factors to the spread are uncertainties from the fitting procedure and the actual variations in the ion distribution over time. Occurrence of the latter is supported by the observations e. g. around 03:00 and between 07:00 - 08:00 where the estimates of $u_{\mathrm{bulk,drift}}$ and $u_{\perp}$ increase/decrease consistently over several successful fits. Visual inspection of the observed and projected distribution functions (Figures 1 and 2, but for the entire observation period) revealed that there are changes in the velocity distribution function on the timescales of individual scans. This includes both changes in the shape of the distribution, as well as changes in the direction of the drift velocity. These changes are not exclusively due to a change in the magnetic field direction because they also appear in the projected velocity distributions. We think that these variations are actual changes in the ion distributions and the entire plasma environment over time.

The parallel velocity component $\mathbf{u}_{\mathrm{bulk},\parallel}$ may be the result of an acceleration along the magnetic field. It may also result from an initial acceleration perpendicular to the magnetic field followed by a change of the magnetic field direction. Such a change of direction is expected around the nucleus due to field line draping. The direction of $\mathbf{u}_{\mathrm{bulk},\parallel}$ gives us an estimate of the upstream magnetic field direction on a spatial scale of the gyroradius. The estimate of $\left|\mathbf{u}_{\mathrm{bulk},\parallel}\right|$ is not well correlated with the $|\mathbf{u}_{\mathrm{bulk,drift}}|$ estimate. This indicates that the mechanisms responsible for acceleration in the gyration plane and perpendicular to it are not coupled. The ambipolar electric field, which is only strong close to the comet nucleus (Vigren & Eriksson, 2019), can provide such an acceleration mechanism. However, as our estimation method relies on the magnetic and electric fields being perpendicular, we cannot characterise the magnetic field-aligned component.

For a larger statistical analysis of cometary pickup ion populations PCA may provide a more efficient way to detect the occurrence of partial ring distributions. A sufficient variance of the individual principal components seems to be a requirement for successful ring fitting. An automated pre-selection based on this criterium will make the assessment of large datasets more feasible than visual inspection alone. Furthermore the last principal component estimate can directly be used as an estimate for the parallel flow direction. This may speed up the fitting procedure, and can also be used to directly calculate the projections for visualisation purposes.

5.2 Electric fields

The local electric field at the comet is important in many ways. It accelerates the newborn ions. Without electric fields, the ions can only change their direction through gyration, not their energy. The gyroradius of newborn ions can only be calculated if we know the electric field in their rest frame. The change between the upstream solar wind electric field and the local cometary electric field shows how shielded the cometary plasma cloud is from the solar wind electric field. In general, wave electric fields can also provide energy to the ions through wave-particle interaction. This mechanism usually happens at frequencies larger than the available time resolution of the ion measurements and can therefore not be assessed with the results presented here.

The anti-sunward component almost always dominates the electric field estimates. This component is larger for the high energy range scans. We identified two possible explanations:

1. The overall electric field strength at the comet is larger for the high energy range scans.

2. The high energy range scans include ions from a larger area around the comet with higher electric fields.

Because the spatial scales for the low energy case are smaller (see gyroradius calculation above) and the distance between spacecraft and nucleus is the same throughout all observations, the high energy scans also sample an area that is slightly further away from the comet nucleus compared to the low energy scans. If the second scenario is correct, this would imply an increase of the anti-sunward electric field further away from the nucleus. It also indicates that the fields are not completely homogeneous over the spatial scales affecting the observed ions. Goetz et al. (2017) provide an estimate for the homogeneity of the magnetic field with respect to cometocentric distance at low outgassing rates. For the solar wind parameters and comet outgassing rates seen in this study, their model predicts a quite stable magnetic field strength from the nucleus up to a distance of approximately 300 km. Further away the magnetic field drops quickly to the magnetic field strength of the undisturbed solar wind. These results indicate that the constant magnetic field assumption is true for about one gyroradius. Variations in the electric field estimate are unlikely to be caused by the magnetic field profile.

We can compare our results to other published electric field estimates for comet 67P at low activity levels. Nilsson et al. (2018) derive an electric field estimate for the entire Rosetta mission. Their estimate was based on a simple analytical model for a cylindrical comet plasma cloud and assumptions about the solar wind electric field. The pickup ion gyroradius was assumed to be much larger than the spatial scale of the cometary plasma. The results show large variabilities over time. For the time period in this study, the magnitude of the electric field estimate is between 0.1 mV/m and 0.8 mV/m. The direction deviates from the anti-sunward direction by 10° to 60°. Now, for the first time, we have estimates of the electric field directly derived from observations. Our results fall within the same range as the model based estimate, with a strong bias towards lower electric field strengths.

Gunell and Goetz (2023) used particle-in-cell modelling to determine the electric fields around the nucleus, and compared with an analytical electric-field model similar to the one in Nilsson et al. (2018). For computational reasons, the nucleus and the entire plasma environment were scaled down by a factor of 200. The fields presented are therefore much larger (up to 1 V/m) compared to reality and can only be compared to our results in direction, not strength. Very close to the nucleus the electric field has a strong anti-sunward component. This is partially retained in the downstream region. However, the convective electric field of the solar wind is the dominant component at 40 km and further away from the nucleus (scaled back to a “real” comet). The heliocentric distance of the comet in their paper is 3 AU, which is larger than in our case. This may explain some of the discrepancies, as the plasma cloud of cometary ions should be larger in our case. In addition to this, the particle-in-cell model uses heavy electrons ($m/m_e = 20$). This further disturbs the spatial scales of the plasma cloud.

In our case the gyroradius is small enough so we can observe a partial gyration of the cometary ions. The estimated drift velocity is perpendicular to the electric field, and the ions are partially magnetised. The resulting electric field is mostly anti-sunward. The same result was also found in previous publications, but in a very different scenario: it was inferred by the motion of the energetic pickup ions, which were travelling anti-sunward according to their calculated bulk velocity moments. This only provides an approximate estimate of the direction of the electric field in the case of very large gyroradii, where all observed energetic pickup ions are accelerated along the electric field. In this scenario, a gyration is not seen in the velocity distribution. If there is a substantial energy-angle dispersion, as in our case, the moment calculations may give inaccurate results. Only in the case of full rings can the bulk drift from moment calculations be used to properly estimate the drift velocity of the distribution.

6 Summary and Conclusions

In alignment with previous observations at Giotto (Coates et al., 1989), we find a clear partial ring-shaped distribution of cometary pickup ions in Rosetta data recorded at comet 67P. Our observations are made at low cometary activity. The plasma environment is much smaller than at 1P/Halley. Instead of fully developed ring distributions we observe newborn cometary ions on the first half of their gyration. These partial rings in velocity space are characterised by their gyration speed $u_\perp$, their bulk drift velocity in the gyration plane $\mathbf{u}_{\mathrm{bulk,drift}}$, and the bulk velocity perpendicular to the gyration plane $\mathbf{u}_{\mathrm{bulk},\parallel}$. The results describe average properties of the plasma environment that are applicable in a region between the solar wind-dominated environment far upstream of the comet, and the plasma environment in the direct vicinity of the nucleus. The clear ring distributions indicate that the fields affecting the cometary pickup ions are sufficiently homogeneous over this spatial scale. After dividing the observations in two groups based on the occurrence of ions with energies $> 200\,\mathrm{eV}$ (high and low energy range observations), we find that the mean of $u_\perp$ and $\mathbf{u}_{\mathrm{bulk,drift}}$ increase for the high energy observations, while that of $\mathbf{u}_{\mathrm{bulk},\parallel}$ does not. This indicates that the additional energy is only distributed in the gyration plane, not in the component along the magnetic field.

Based on the gyroradii estimates (average: 340 km), we expect this region to be a few hundreds of km in size. There is a large discrepancy between the expected gyroradius of water-group pickup ion in the undisturbed solar wind ($\approx 10\,000\,\mathrm{km}$) and the value found here. The comet plasma cloud partially shields the inner part of the coma from the solar electric field. This lower electric field strength, in combination with the increased magnetic field due to pile-up closer to the nucleus, results in much smaller ion gyroradii.

We furthermore estimate the electric field at the comet based on this homogeneous-field assumption. The resulting electric field is mostly directed anti-sunward. The average strength is $0.21\,\mathrm{mV/m}$, and increases from $0.16\,\mathrm{mV/m}$ to $0.24\,\mathrm{mV/m}$ when splitting the observations in a low and high energy range. The anti-sunward component ($-E_x$) increases for the high energy observations, while the perpendicular component (E_y) remains the same. The larger gyroradii associated with the high energy observations could indicate that the homogeneous-field assumption breaks down for the ions born furthest away from the observation point. In this scenario, the electric field is still directed anti-sunward further away from the nucleus, but less shielded by the cometary plasma cloud. The strength is therefore higher.

Another estimate for the average electric field direction is available from the solar wind proton distributions (see Moeslinger et al., 2023). Because of the larger velocities and therefore larger gyroradii, these estimates are representative of an even larger spatial scale in the upstream region of the nucleus. The fields close to the nucleus are not expected to have a significant impact on this estimate. The direction of this electric field is roughly perpendicular to the anti-sunward field close to the nucleus presented here (not shown). This is in agreement with the expected convective electric field of the upstream solar wind in the comet reference frame. The effects of the transition region between these two fields should be analysed more carefully, e. g. using simulations, in a future study. Furthermore, we mainly used the shape of the velocity distribution to estimate the electric fields in this paper. Nilsson et al. (2018) also provided another way to estimate the electric field strength by relating the measured flux of particles with their energy as a proxy for their origin. Using the results of this paper, we can also backtrace the observed particles to the approximate location of where they were ionised. Combining both approaches in a future study would help to refine the electric field measurements, and refine the validity of the homogeneous-field assumption.

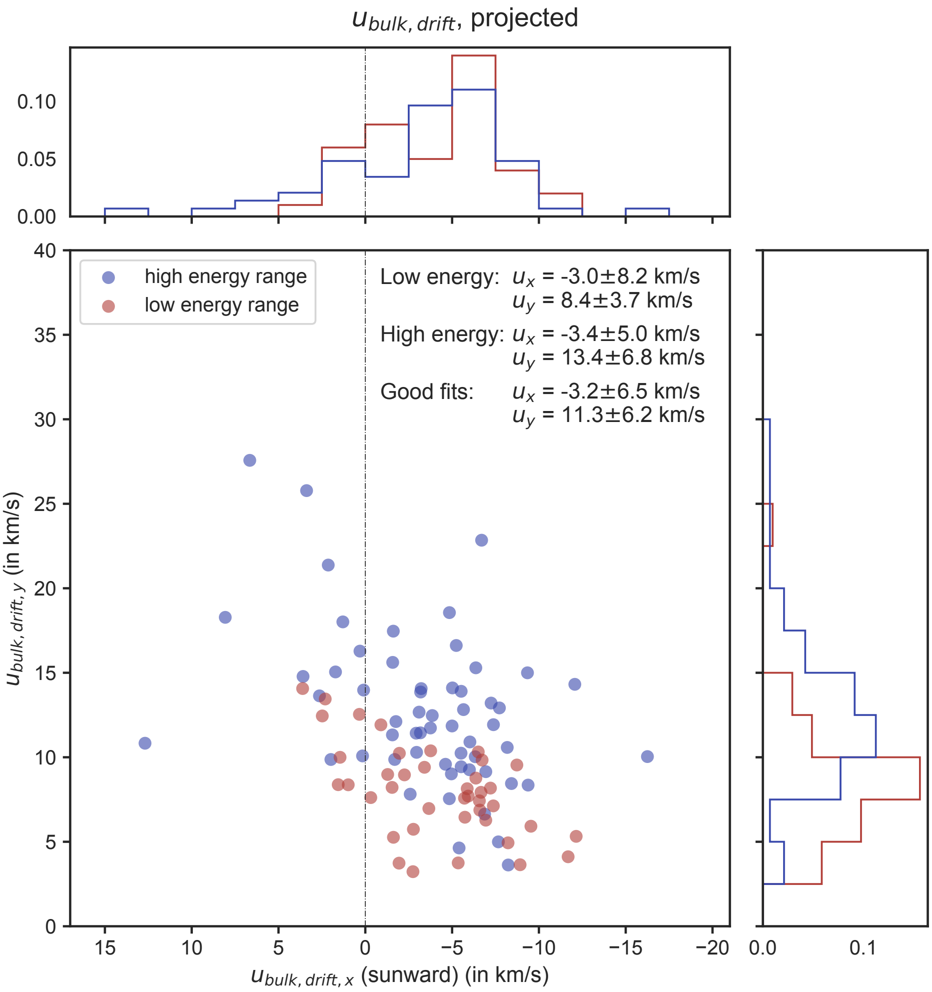

Figure A1. Scatter plot of the fitted drift velocity $\mathbf{u}_{\mathrm{bulk,drift}}$, projected into the same cartesian coordinate system as Figures 2 and 4. In this coordinate system, the z-component is always 0.

Appendix A Direction of $\mathbf{u}_{\mathrm{bulk,drift}}$

Figure A1 shows the direction of the fitted drift velocity $\mathbf{u}_{\mathrm{bulk,drift}}$ of all successful fits. The individual scans are projected into the cartesian coordinate system as described in Section 3.2. The average velocity is $[-3.2, 11.3, 0]$ km/s for good fits, so the dominant component is along the y-axis. In agreement with the electric field estimates (Figure 4), the average value of the y-component increases for the high energy scans, compared to the low energy scans. There is no significant difference found in the x-component of the same data.

Appendix B Data Availability Statement

The data used in this study is available through the ESA Planetary Science Archive (ESA PSA) and NASA Planetary Data System (NASA PDS). For RPC-ICA, the mass-separated dataset (Nilsson, 2021) was used. Magnetic field data (RPC-MAG) was obtained from Richter et al. (2019). Data analysis was done using NumPy version 1.20.2 (Harris et al., 2020). Figures were made using Matplotlib (Caswell et al., 2021; Hunter, 2007) and Colorspacious (Smith, 2015).

Acknowledgments

Rosetta is a European Space Agency (ESA) mission with contributions from its member states and the National Aeronautics and Space Administration (NASA). Work at the Swedish Institute of Space Physics in Kiruna (IRF) was funded by the Swedish National Space Agency (SNSA) grant 132/19. Work at Umeå university was supported by the SNSA grant 108/18.

References

Berčič, L., Behar, E., Nilsson, H., Nicolaou, G., Wieser, G. S., Wieser, M., & Goetz, C. (2018, 5). Cometary ion dynamics observed in the close vicinity of comet 67p/churyumov-gerasimenko during the intermediate activity period. *Astronomy and Astrophysics*, *613*. doi: 10.1051/0004-6361/201732082

Beth, A., Galand, M., Nilsson, H., Goldstein, R., Mokashi, P., Eriksson, A., ... Allen, T. (2019, 9). *RPC User Guide Version 3.* Retrieved from `https://cosmos.esa.int/web/psa/rosetta`

Bieler, A., Altwegg, K., Balsiger, H., Berthelier, J. J., Calmonte, U., Combi, M., ... Wurz, P. (2015, 11). Comparison of 3d kinetic and hydrodynamic models to rosina-cops measurements of the neutral coma of 67p/churyumov-gerasimenko. *Astronomy and Astrophysics*, *583*. doi: 10.1051/0004-6361/201526178

Carr, C., Cupido, E., Lee, C. G. Y., Balogh, A., Beek, T., Burch, J. L., ... Trotignon, J. G. (2007). Rpc: The rosetta plasma consortium. *Space Science Reviews*, *128*(1), 629–647. Retrieved from `https://doi.org/10.1007/s11214-006-9136-4` doi: 10.1007/s11214-006-9136-4

Caswell, T. A., Lee, M. D. A., de Andrade, E. S., Hunter, J., Hoffmann, T., Firing, E., ... Ivanov, P. (2021). *matplotlib/matplotlib: REL: v3.4.1* [software]. Retrieved from `https://github.com/matplotlib/matplotlib/tree/v3.4.1` doi: 10.5281/zenodo.4649959

Coates, A. J., Johnstone, A. D., Wilken, B., Jockers, K., & Glassmeier, K.-H. (1989, 8). Velocity space diffusion of pickup ions from the water group at comet halley. *Journal of Geophysical Research: Space Physics*, *94*, 9983-9993. doi: 10.1029/ja094ia08p09983

Filacchione, G., Groussin, O., Herny, C., Kappel, D., Mottola, S., Oklay, N., ... Raponi, A. (2019, 1). *Comet 67p/cg nucleus composition and comparison to other comets* (Vol. 215). Springer Netherlands. doi: 10.1007/s11214-019-0580-3

Galand, M., Héritier, K. L., Odelstad, E., Henri, P., Broiles, T. W., Allen, A. J., ... Wurz, P. (2016). Ionospheric plasma of comet 67p probed by rosetta at 3 au from the sun. *Monthly Notices of the Royal Astronomical Society*, *462*, S331-S351. doi: 10.1093/mnras/stw2891

Glassmeier, K., Neubauer, F., Acuna, M., & Mariani, F. (1987). Low-frequency magnetic field fluctuations in comet P/Halley's magnetosheath: Giotto observations. *Astronomy & Astrophysics*.

Glassmeier, K.-H., Boehnhardt, H., Koschny, D., Kührt, E., & Richter, I. (2007). The Rosetta Mission: Flying Towards the Origin of the Solar System. *Space Science Reviews*, *128*(1-4), 1-21. Retrieved from `http://dx.doi.org/10.1007/s11214-006-9140-8` doi: 10.1007/s11214-006-9140-8

Glassmeier, K.-H., Richter, I., Diedrich, A., Musmann, G., Auster, U., Motschmann, U., ... others (2007). Rpc-mag the fluxgate magnetometer in the rosetta plasma consortium. *Space Science Reviews*, *128*(1), 649–670.

Goetz, C., Behar, E., Beth, A., Bodewits, D., Bromley, S., Burch, J., … Volwerk, M. (2022, 12). The plasma environment of comet 67p/churyumov-gerasimenko. *Space Science Reviews*, *218*. doi: 10.1007/s11214-022-00931-1

Goetz, C., Volwerk, M., Richter, I., & Glassmeier, K. H. (2017, 7). Evolution of the magnetic field at comet 67p/churyumov-gerasimenko. *Monthly Notices of the Royal Astronomical Society*, *469*, S268-S275. doi: 10.1093/mnras/stx1570

Gunell, H., & Goetz, C. (2023). Particle-in-cell modelling of comet 67p/churyumov-gerasimenko spatial structures of densities and electric fields. *Astronomy & Astrophysics*, *674*, A65. doi: 10.1051/0004-6361/202245197

Harris, C. R., Millman, K. J., van der Walt, S. J., Gommers, R., Virtanen, P., Cournapeau, D., … Oliphant, T. E. (2020, September). Array programming with NumPy. *Nature*, *585*(7825), 357–362. Retrieved from `https://doi.org/10.1038/s41586-020-2649-2` doi: 10.1038/s41586-020-2649-2

Hunter, J. D. (2007). Matplotlib: A 2d graphics environment. *Computing in Science & Engineering*, *9*(3), 90–95. doi: 10.1109/MCSE.2007.55

Moeslinger, A., Wieser, G. S., Nilsson, H., Gunell, H., Williamson, H. N., LLera, K., … Richter, I. (2023, 2). Solar wind protons forming partial ring distributions at comet 67p. *Journal of Geophysical Research: Space Physics*, *128*. doi: 10.1029/2022JA031082

Neugebauer, M., Lazarus, A., Balsiger, H., Fuselier, S., Neubauer, F., & Rosenbauer, H. (1989). The velocity distributions of cometary protons picked up by the solar wind. *Journal of Geophysical Research: Space Physics*, *94*(A5), 5227-5239. Retrieved from `https://agupubs.onlinelibrary.wiley.com/doi/abs/10.1029/JA094iA05p05227` doi: https://doi.org/10.1029/JA094iA05p05227

Nilsson, H. (2021). *ROSETTA-ORBITER 67P RPCICA 4 EXT2 RESAMPLED AND CALIBRATED V1.0* [dataset]. ESA Planetary Science Archive and NASA Planetary Data System. Retrieved from `https://pdssbn.astro.umd.edu/holdings/ro-c-rpcica-4-ext2-phys-mass-v1.0/dataset.shtml`

Nilsson, H., Behar, E., Burch, J. L., Carr, C. M., Eriksson, A. I., Glassmeier, K. H., … Karlsson, T. (2021, 1). *Birth of a magnetosphere.* wiley. doi: 10.1002/9781119815624.ch27

Nilsson, H., Gunell, H., Karlsson, T., Brenning, N., Henri, P., Goetz, C., … Vallières, X. (2018, 8). Size of a plasma cloud matters: The polarisation electric field of a small-scale comet ionosphere. *Astronomy and Astrophysics*, *616*. doi: 10.1051/0004-6361/201833199

Nilsson, H., Lundin, R., Lundin, K., Barabash, S., Borg, H., Norberg, O., … Burch, J. L. (2007, 5). Rpc-ica: The ion composition analyzer of the rosetta plasma consortium. *Space Science Reviews*, *128*, 671-695. doi: 10.1007/s11214-006-9031-z

Nilsson, H., Williamson, H. N., Bergman, S., Stenberg Wieser, G., Wieser, M., Behar, E., … Goetz, C. (2020, 09). Average cometary ion flow pattern in the vicinity of comet 67P from moment data. *Monthly Notices of the Royal Astronomical Society*, *498*(4), 5263-5272. Retrieved from `https://doi.org/10.1093/mnras/staa2613` doi: 10.1093/mnras/staa2613

Reinhard, R. (1987, jun). The giotto mission to comet halley. *Journal of Physics E: Scientific Instruments*, *20*(6), 700–712. Retrieved from `https://doi.org/10.1088/0022-3735/20/6/029` doi: 10.1088/0022-3735/20/6/029

Richter, I., Glassmeier, K.-H., Goetz, C., Koenders, C., Eichelberger, H., & Cupido, E. (2019). *ROSETTA-ORBITER 67P RPCMAG 3 EXT2 CALIBRATED V9.0* [dataset]. ESA Planetary Science Archive and NASA Planetary Data System. Retrieved from `https://pdssbn.astro.umd.edu/holdings/ro-c-rpcmag-3-ext2-calibrated-v9.0/dataset.shtml`

Smith, N. J. (2015). *Colorspacious* [software]. Retrieved from `https://colorspacious.readthedocs.io/en/latest/overview.html` doi: 10.5281/zenodo.1214904

Vigren, E., & Eriksson, A. I. (2019, 1). On the ion-neutral coupling in cometary comae. *Monthly Notices of the Royal Astronomical Society*, *482*, 1937-1941. doi: 10.1093/mnras/sty2869

Williamson, H. N., Nilsson, H., Stenberg Wieser, G., A. Moeslinger, A., & Goetz, C. (2022, 4). Development of a cometosheath at comet 67p/churyumov-gerasimenko a case study comparison of rosetta observations. *A&A*, *660*. Retrieved from `https://doi.org/10.1051/0004-6361/202142461` doi: 10.1051/0004-6361/202142461